

Unstable flow structures in the Blasius boundary layer^{*}

H. Wedin^{1,a}, A. Bottaro¹, A. Hanifi^{2,3}, and G. Zampogna¹

¹ Department of Civil, Chemical and Environmental Engineering, University of Genova, Via Montallegro 1, 16145 Genova, Italy

² Swedish Defence Research Agency (FOI), SE-164 90 Stockholm, Sweden

³ Linné FLOW Centre, Dept. of Mechanics, KTH Royal Institute of Technology, SE-100 44 Stockholm, Sweden

Received 28 June 2013 and Received in final form 15 November 2013

Published online: 28 April 2014 – © EDP Sciences / Società Italiana di Fisica / Springer-Verlag 2014

Abstract. Finite amplitude coherent structures with a reflection symmetry in the spanwise direction of a parallel boundary layer flow are reported together with a preliminary analysis of their stability. The search for the solutions is based on the self-sustaining process originally described by Waleffe (Phys. Fluids **9**, 883 (1997)). This requires adding a body force to the Navier-Stokes equations; to locate a relevant nonlinear solution it is necessary to perform a continuation in the nonlinear regime and parameter space in order to render the body force of vanishing amplitude. Some states computed display a spanwise spacing between streaks of the same length scale as turbulence flow structures observed in experiments (S.K. Robinson, Ann. Rev. Fluid Mech. **23**, 601 (1991)), and are found to be situated within the buffer layer. The exact coherent structures are unstable to small amplitude perturbations and thus may be part of a set of unstable nonlinear states of possible use to describe the turbulent transition. The nonlinear solutions survive down to a displacement thickness Reynolds number $Re_* = 496$, displaying a 4-vortex structure and an amplitude of the streamwise root-mean-square velocity of 6% scaled with the free-stream velocity. At this Re_* the exact coherent structure bifurcates supercritically and this is the point where the laminar Blasius flow starts to cohabit the phase space with alternative simple exact solutions of the Navier-Stokes equations.

1 Introduction

Transitional and turbulent flows take place in many technical applications such as the flow over an airplane wing or around a car body. Getting a fundamental insight on turbulent flows or understanding how a flow undergoes transition to turbulence is of great significance since a wide range of practical flows occur in non-laminar conditions, and may lead to ideas on how to control it. The boundary layer flow on a flat plate is of great fundamental as well as practical importance. Ever since the pioneering experimental study of pipe flow by Reynolds [1] the question of how a turbulent flow arises and sustains itself is still not completely understood even though the past two decades have witnessed progress on this subject. In terms of dynamical system theory, in the end of the 19th century Poincaré [2] established that chaotic dynamics is generated by the interplay of locally unstable states and the interweaving of their stable and unstable manifolds. Some important steps on how a fluid flow becomes turbulent were laid by the theories of Landau [3] and Hopf [4]. To describe the route to turbulence the linearly unsta-

ble laminar flow is thought to go through an infinite well defined sequence of bifurcations, or sudden changes, giving rise to increasingly complex states for increasing flow speed. Later it was shown by Ruelle and Takens [5], see also later extension by Newhouse *et al.* [6], that a *strange* attractor arises after a small number of bifurcations. An attractor can be a stable fixed point or a stable limit cycle, and shows exponential sensitive dependence on initial conditions [7]. An experiment on the Taylor-Couette flow system confirmed the Ruelle-Takens scenario of the turbulent transition [8]. Some early intuition about the dynamics of nonlinear systems was achieved by Lorenz [9], simulating a flow using a highly truncated version of the Navier-Stokes equations. Lorenz discovered that the flow never positioned itself on a fixed point or ended up as a periodic solution as $t \rightarrow \infty$; instead the trajectories in phase space never repeated themselves showing a chaotic motion on a strange attractor (term later coined by Ruelle and Takens [5]). He realised that a small variation in the initial conditions quickly gave rise to large changes in the behavior of the flow at later times, a fact referred to as “sensitive dependence on initial conditions”, and is due to the nonlinearity of the governing equations. Although the flow seemed chaotic it had structure in the sense that starting from two different initial conditions the flow would still traverse the same attractor. In numerical

^{*} Contribution to the Topical Issue “Irreversible Dynamics: A topical issue dedicated to Paul Manneville” edited by Patrice Le Gal and Laurette S. Tuckerman.

^a e-mail: hakanwedin@hotmail.com

studies it has been shown that neighbouring trajectories diverge exponentially, where the Lyapunov exponent defines the rate of separation [10]. For the intermittent transition route to chaos [11] the attractor is a periodic orbit as long as a parameter value, *e.g.* the Reynolds number is lower than a critical value Re_c . Going slightly past Re_c the flow is quasi-periodic with bursts of limited duration that bring the flow off the periodic orbit. Finally for Re considerably larger than Re_c the flow is in a more or less constant state of bursts which then defines a new flow distinct from the periodic motion at $Re < Re_c$. The above scenario is demonstrated on the Lorenz system in [11] for increasing values of a control parameter.

In the past ten years the pipe flow configuration has been subject to extensive studies, both numerical and experimental. To understand the turbulence transition the pipe flow can be considered as a nonlinear dynamical system where the state is governed by $\dot{\mathbf{u}} = \mathcal{N}(\mathbf{u}, Re)$, with \mathcal{N} being the remainder terms of the incompressible Navier-Stokes equations. Since the laminar parabolic flow profile is asymptotically stable to small perturbations [12, 13] the theory of the route to chaos cannot be used in the form elaborated by [5]. The lower limit for triggering transition corresponds to $Re \approx 1800$ – 2000 , and at low Reynolds numbers a finite amplitude perturbation suffices to trigger transition, as shown by several experiments [14–17], highlighting the nonlinear nature of the transition process. Having earlier research findings on strange attractors in mind, one might expect that above a certain flow rate a turbulent attractor would appear and that the turbulent dynamics would be maintained there permanently by the appearance of fixed points or limit cycles such as unstable nonlinear travelling wave solutions. On the other hand the experiments by Darbyshire and Mullin [14] indicated no distinctive boundary between initial perturbations leading either to laminar flow or turbulence. This suggests the formation of a transient strange saddle (*i.e.* a chaotic saddle or a non-attracting chaotic set), rather than a strange attractor, *i.e.* the so-called chaotic saddle “leaks” and the flow, after having spent some time in the neighbourhood of this non-attracting chaotic set, can revert to a non-chaotic attractor such as the laminar flow. By increasing the flow rate, does the strange saddle go through some kind of an inverse boundary crisis [7] and thus becomes a chaotic attractor? There have been a number of suggestions to answer this question; several studies have shown that there is a threshold for the transition from transient to permanent turbulent flow at $1750 < Re = Re_c < 1870$ [18, 19] and recently Avila *et al.* [20] have argued that turbulence becomes sustained at $Re = 2040 \pm 10$.

The stability border in phase space, called the edge of chaos, has received quite some attention recently; the edge is that hyper-surface that separates initial conditions that bring the flow to turbulence from those which decay to the laminar solution. On this separatrix relative attractors named edge states might exist and they are relevant to understand the transition to turbulence. The edge states can have various characteristics such as being a travelling wave, a relative periodic orbit, a fixed point or a flow field

that holds chaotic dynamics [21–24]. The edge of chaos in the Blasius boundary layer configuration has been studied in [25, 26] and [27] with spatially evolving flow simulations.

The laminar Blasius boundary layer flow over a flat plate is defined by two velocity components $U(x, y)$, $V(x, y)$, with x being the streamwise direction and y normal to the wall. The study of the linear stability, that is the asymptotic behavior of the least stable single-mode perturbation as $t \rightarrow \infty$ [28], of a parallel laminar boundary layer has shown that two-dimensional Tollmien-Schlichting waves (T-S waves) begin to amplify at $Re_* = 519.4$ (based on the displacement thickness δ_* , free-stream speed U_∞ and the kinematic viscosity ν). The parallel flow approximation is a valid approximation for sufficiently large Re_* since the wall-normal laminar flow component V is of order $1/Re_*$. The numerical simulation of the complete Navier-Stokes equations of a small amplitude wave (non-parallel effects accounted for) showed that locally parallel theory predicts Fourier amplitude functions well [29]. It was shown that the non-parallel effects do not fully account for the disagreement observed elsewhere on the neutral curves between experimental and theoretical parallel theory. Their results went along with the conclusion of [30] therefore justifying the use of the parallel flow assumption. The threshold for monotonic decay, shown to be $Re_* = 17$ [25], refers to the lower limit where short-lived growth of disturbance energy is possible; the lower limit of sustained turbulence is $Re_* = 390$ – 400 [25, 31]. Apart from the mechanism of the linear exponential amplification of T-S waves there is a possibility of transient growth whenever the nature of the linearised stability operator is non-normal. This implies that even though the linear asymptotic theory indicates that the system is stable, short-lived growth of several orders of magnitude is possible that may trigger nonlinear effects (see *e.g.* [32–36]). In most cases, the optimal disturbances, yielding the maximum growth, are steady streamwise independent vortices, but when used as initial conditions in numerical simulations they do not necessarily trigger transition to turbulence in the most efficient way [37].

The experimental study by [38] observed wavy unstable coherent structures in turbulent boundary layers, a sign of a hidden regularity within turbulence. This suggests that progress in the understanding of turbulence can be achieved by searching for elementary nonlinear solutions of small scale which are maintained within the flow. This provides a connection to the self-sustaining process (SSP) outlined by Waleffe [39]. The SSP has been used several times for discovering numerical large-scale nonlinear coherent structures (commonly called ECS for exact coherent structures), mostly for systems that are linearly stable, and covers various types of solutions in canonical flows such as steady states and TWS (for “travelling wave solutions”) in various configurations [40–47]. Other similar studies include [48] where the natural bifurcation point of the system was used to initiate the bifurcation into the nonlinear regime, and [49] and [50] where a homotopy approach in a physical system was used to find the ECS, rather than the SSP. The fact is that these so-

lutions are believed to be unstable in general (see *e.g.* [51] and [50]), with usually only a few unstable directions and many stable ones, rendering it difficult to detect them in experiments or direct numerical simulations. The instability causes the flow to bounce back and forth between the nonlinear solutions possibly embedded in a chaotic saddle. Similar transient flow structures have been detected in experiments by [52, 53] showing their relevance. On the other hand, in [51] a $5D$ and a $10D$ long pipe in a turbulent state ($Re = 2400$) showed that recurrent visits to travelling waves occurred for solutions with low to intermediate wall shear stress and for no more than 10% of the time considered. In [54] it was found that the currently known ECS in pipe flow sit in a less energetic region between the laminar and turbulent flow, suggesting that the ECS are important for the transitional phase rather than the fully turbulent flow, at least for the pipe flow configuration. The edge of chaos is highly related to the turbulent transition, numerical studies of the edge in pipe flow such as the one of Duguet *et al.* [24] observed attracting travelling wave states embedded in this separatrix, which actually turned out to be the asymmetric TWS discovered by Pringle and Kerswell [55]. The same was observed by Schneider *et al.* [23], although for the plane Couette flow, where the edge-tracking technique converged to a constant energy invariant solution. Usually the TWS are lower branch solutions of lower energy than the corresponding higher amplitude solutions sitting on the upper branch. Starting on either side of the stable manifold of the lower branch travelling wave the flow would approach the turbulent state or alternatively revert to laminar flow as shown by Wang *et al.* [56], hence demonstrating the relevance of the TWS to the transition. The experimental study of de Lozar *et al.* [57] shares the same conclusion revealing two unstable travelling waves in decaying pipe turbulence, and therefore suggesting that the TWS are building block of turbulence transition. By taking two different snapshots of the experimental flow field as initial conditions they found two converged numerical TWS corresponding to those named S1 and M1 in [44]. However, some of the waves on the upper branch of [44] go against the hypothesis that the TWS are only important for the transition phase by displaying very high wall shear stresses, thus making them possibly interesting also as descriptors for turbulence. The travelling waves are relative equilibrium points in phase space at fixed energy content. To get detailed knowledge of the physical mechanisms behind the maintenance of turbulence it is probably preferable to focus on exact coherent structures in the shape of periodic orbits, such as those discovered in [58] and [59]. Another example of these solutions are those that sit on the edge of chaos, as studied in [60] for the asymptotic suction boundary layer, which show strong time-periodic bursts with a travelling-wave-like behaviour. For the asymptotic suction boundary layer at subcritical Reynolds numbers and in domains sufficiently wide and long, Khapko *et al.* [61] observe three edge state solutions (for different initial conditions) localised in the spanwise direction. They are periodic or-

bits going through recurring bursts, similar to the regeneration cycle described in [39, 62, 63]. Bringing down the length of the domain the localised edge states turn chaotic. To further the understanding of turbulent patches one needs localized exact numerical solutions. Spanwise localized states have previously been discovered by Schneider *et al.* [64]. Continuing in the Reynolds number the solution turned out to connect with the globally periodic equilibrium state of [49]. In [65] streamwise localized solutions are extracted from the Navier-Stokes equations, showing flow structures very similar to turbulent puffs.

The aim of this paper is to search for three-dimensional nonlinear exact coherent structures with the purpose to find solutions that may have pertinence to the transition to turbulence. Relevant and similar studies to the present one have been carried out by [66–68] and [69] (with a compliant coating) which focused on nonlinear two-dimensional solutions to the Blasius boundary layer flow. In [68] the mapping out of the neutral surface was followed up by a secondary stability analysis of the nonlinear solutions. Rotenberry [66] found that the minimum Re_* of the nonlinear Tollmien-Schlichting waves was about 510 slightly below the linear critical point at 519.4. To find a key to the transition mechanism, with the hope to clarify the bursting process, Ehrenstein and Koch [70] performed a secondary stability analysis of the two-dimensional nonlinear equilibrium solutions. Other studies on the boundary layer flow are due to Koch *et al.* [71]; they reported three-dimensional nonlinear equilibrium states for the flow over an infinite swept flat plate. The fact that the ECS can reproduce key features of the transition to turbulence could thus provide us with the essential elements for understanding the dynamics of chaotic flows. This can set the basis for a dynamical-system-theory of turbulence [72] with perhaps outlooks also on flow control.

The paper is organised as follows: in sect. 2 we present the laminar flow, the equations governing the perturbation that is imposed on the laminar flow, the numerical expression of the perturbation and various physical quantities. In sect. 3 the results are presented using the self-sustaining process outlined by Waleffe [39], resulting in ECS in the shape of travelling wave solutions. Section 4 is concerned with the linear stability of the travelling waves. Concluding remarks and discussion are provided in sect. 5.

2 Definitions

The flow over a flat plate in an isothermal incompressible boundary layer at zero angle of incidence, zero free-stream turbulence and zero pressure gradient is studied (cf. fig. 1). The aim is to find three-dimensional nonlinear solutions of the Blasius boundary layer flow using bifurcation theory. The objective is to study the pre-transitional or transitional behavior to find where in parameter space one can expect to observe changes from the laminar profile to solutions that might be related to the transition process. As the uniform flow encounters the plate a laminar boundary layer starts to grow. The leading edge is situated at

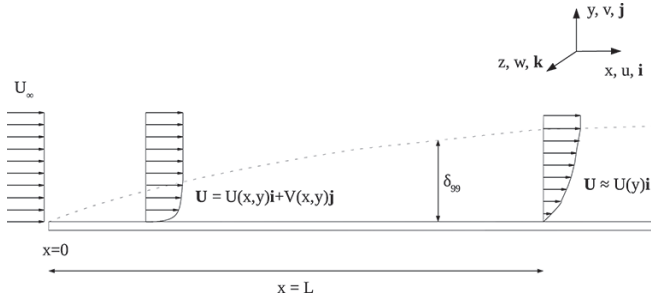


Fig. 1. The laminar flow in a boundary layer. The boundary layer thickness is denoted by δ_{99} and L is the distance from the leading edge. At low Re , or equivalently at small x , the Blasius flow is 2-dimensional; for sufficiently large Re (at $x = L$) the contribution from the wall-normal component $V(x, y)$ is small, hence one can assume a local unidirectional flow.

$\hat{x} = 0$ and the plate is considered to be infinite in both the \hat{x} -direction and the \hat{z} -direction and located at $\hat{y} = 0$. The infinite outer edge of the flow domain is truncated to the computational domain $\hat{y} = \hat{y}_{\max}$. In cases with low ambient turbulent fluctuations, transition may occur due to the growth of Tollmien-Schlichting waves generated *e.g.* by the interaction of acoustic perturbations with the leading edge or with surface inhomogeneities. Transition can also be triggered by free-stream fluctuations of sufficient amplitude where the initial growth of the flow structures can be successfully explained by the mechanism of non-modal or transient growth [73]. All free-stream parameters are denoted by ∞ and dimensional variables by “ $\hat{}$ ”. The unit vectors are \mathbf{i} , \mathbf{j} and \mathbf{k} and the velocity vector is defined as $\hat{\mathbf{u}} = \hat{u}\mathbf{i} + \hat{v}\mathbf{j} + \hat{w}\mathbf{k}$ represented by the streamwise, wall-normal and spanwise component, respectively, the pressure as \hat{p} , $\hat{\nu}$ the kinematic viscosity and time \hat{t} . The involved variables are non-dimensionalised using the unidirectional free-stream speed \hat{U}_{∞} , density $\hat{\rho}$ and the reference length scale $\hat{\delta}_0 = (\hat{x}_0 \hat{\nu}_0 / \hat{U}_{\infty})^{1/2}$. The Blasius boundary layer thickness $\hat{\delta}_{99}$ is defined as the distance from the wall where the boundary layer flow is 99% of the free-stream speed \hat{U}_{∞} (see fig. 1), and $\hat{\delta}_{99} \approx 5\hat{\delta}$. We non-dimensionalise in the following way:

$$\mathbf{u} = \frac{\hat{\mathbf{u}}}{\hat{U}_{\infty}}, \quad \mathbf{x} = \frac{\hat{\mathbf{x}}}{\hat{\delta}_0}, \quad p = \frac{\hat{p}}{\hat{\rho}\hat{U}_{\infty}^2}, \quad t = \frac{\hat{t}\hat{U}_{\infty}}{\hat{\delta}_0}. \quad (1)$$

The local Reynolds number is defined as $Re = \hat{U}_{\infty}\hat{\delta}_0/\hat{\nu} = (\hat{U}_{\infty}\hat{x}/\hat{\nu})^{1/2}$ and $Re_x = \hat{U}_{\infty}\hat{x}/\hat{\nu}$.

2.1 The laminar flow

We consider the laminar Blasius solution which is two-dimensional and equal to $\hat{\mathbf{U}}(\hat{x}, \hat{y}) = \hat{U}(\hat{x}, \hat{y})\mathbf{i} + \hat{V}(\hat{x}, \hat{y})\mathbf{j}$ obtained from the well-known Blasius boundary layer equation

$$f_{\eta\eta\eta} + \frac{1}{2}ff_{\eta\eta} = 0, \quad (2)$$

where $f = f(\eta)$ and $f_{\eta} = df/d\eta$, the boundary condi-

tions $f(0) = 0$, $f_{\eta}(0) = 0$ and $f_{\eta}(\eta_{\max}) = 1$. The non-dimensional self-similar coordinate η accounts for both the dimensional coordinates \hat{x} and \hat{y} and is defined as $\eta = \hat{y}[\hat{U}_{\infty}/(\hat{\nu}\hat{x})]^{1/2}$. The laminar flow components on account of f are

$$\hat{U}(\hat{x}, \hat{y}) = \hat{U}_{\infty}f_{\eta},$$

$$\hat{V}(\hat{x}, \hat{y}) = \left(\frac{\hat{U}_{\infty}\hat{\nu}}{4\hat{x}}\right)^{1/2} (\eta f_{\eta} - f) = \frac{\hat{U}_{\infty}}{2Re} (\eta f_{\eta} - f). \quad (3)$$

It is also worth noting that the boundary-layer theory is not valid near the leading edge since there the assumption $\partial_{\hat{y}} \gg \partial_{\hat{x}}$ is not correct. According to Munson *et al.* [74] the theory is valid for Re above 30. In non-dimensional form the laminar flow is represented as (U, V) ; in this study we use the parallel-flow approximation or $V = 0$, *i.e.* a parallel laminar flow so that $\mathbf{U} = U(y)\mathbf{i} = f_{\eta}(y)\mathbf{i}$, this implies a non-thickening boundary layer. The parallel flow assumption is valid for Re sufficiently large, to approximate the non-parallel Blasius flow. The validity of this supposition is confirmed by the numerical simulation of [29] and the experiments by [30]. A forcing term ($= -Re^{-1}U_{yy}(y)$) needs to be added to the streamwise dimensionless momentum equation to account for the parallel base flow [66, 67].

2.2 The perturbation

To search for three-dimensional solutions we superimpose a perturbation $\mathbf{u}' = (u', v', w')$ and p' on the parallel laminar base flow. The total velocity vector is $\mathbf{u} = U\mathbf{i} + \epsilon\mathbf{u}'$; the governing equations for the perturbation are

$$\mathbf{u}'_t + \nabla p' - \frac{1}{Re} \nabla^2 \mathbf{u}' + (U \cdot \nabla) \mathbf{u}' + (\mathbf{u}' \cdot \nabla) U = -\epsilon \mathbf{u}' \cdot \nabla \mathbf{u}', \quad (4)$$

$$\nabla \cdot \mathbf{u}' = 0, \quad (5)$$

where ϵ is an amplitude. In the free-stream we have the physically realistic boundary condition of uniform constant flow, $\mathbf{u} = (1, 0, 0)$; at the plate we have vanishing velocity, $\mathbf{u}(t, x, y = 0, z) = \mathbf{0}$. Since U is a function of y we can assume periodicity and take \mathbf{u}' to be a travelling wave separable in x, z and t . The disturbance is thus expressed as

$$\mathbf{u}' = \sum_{b=-NX}^{NX} \sum_{j=-NZ}^{NZ} \tilde{\mathbf{u}}^{(bj)}(y) e^{Ij\beta z} e^{Ib\alpha(x-ct)} = \sum_{b=-NX}^{NX} \sum_{j=-NZ}^{NZ} \sum_{i=0}^{NY} \hat{\mathbf{u}}_{bji} T_i(y) e^{Ij\beta z} e^{Ib\alpha(x-ct)}, \quad (6)$$

with the $T_i(y)$ the Chebyshev polynomial and the imaginary unit $I = \sqrt{-1}$, α and β are real wave numbers, setting the wavelength $\lambda_x = 2\pi/\alpha$ and $\lambda_z = 2\pi/\beta$, and yielding a periodicity of the perturbation as $\mathbf{u}'(x, y, z, t) =$

$\mathbf{u}'(x+2\pi/\alpha, y, z, t)$ and $\mathbf{u}'(x, y, z, t) = \mathbf{u}'(x, y, z+2\pi/\beta, t)$. The eigenvalue $c = c_r + I c_i$ is generally complex (forced real for the nonlinear study where c_r is the wave speed). A time-independent problem is considered by viewing the system in a frame of reference $x - c_r t \rightarrow X$ moving with the wave speed c_r , hence $\partial_t \rightarrow -c_r \partial_X$. At the outer edge of the computational domain $y = y_{\max}$ we impose asymptotically decaying disturbances or $\tilde{\mathbf{u}}_y^{(bj)} + (b^2 \alpha^2 + j^2 \beta^2)^{1/2} \tilde{\mathbf{u}}^{(bj)} = \mathbf{0}$, where b and j are the indices shown in eq. (6). The $\tilde{u}^{(0,0)}(y)$ mode does not decay exponentially to zero and is thus finite with zero gradient at $y = y_{\max}$, *i.e.* we impose for this particular Fourier component the Neumann boundary condition $d\tilde{u}^{(0,0)}/dy = 0$ at $y = y_{\max}$. This asymptotic boundary condition was also imposed in the two-dimensional study by Koch [68] for the Blasius boundary layer; as a result the mean flow deviation $\tilde{u}^{(0)}(y)$ was observed to be still finite at $y = y_{\max}$. Knowing the free-stream conditions given above, the base flow U needs to act as a corrector to ensure unperturbed flow at the outer edge of the domain. The base flow is therefore set equal to

$$U(y) = (1 + \epsilon K) f_\eta(\eta) = K_p f_\eta(\eta). \quad (7)$$

The physical idea behind this is that the coefficient K_p serves to ensure that the correct asymptotic boundary condition is satisfied, *i.e.* to maintain the uniform flow at $y = y_{\max}$ constant even in the presence of finite amplitude perturbations [66–69]. We have $K_p = 1$ for purely laminar flow and infinitesimal disturbances, while K_p is different from unity in the presence of finite amplitude perturbations. This is ensured by imposing the following equation involving the $b = j = 0$ -mode of the u -perturbation:

$$K_p + \epsilon \tilde{u}^{(0,0)}(y = y_{\max}) = 1, \quad (8)$$

and is simply derived from the given free-stream condition $\mathbf{u} = (1, 0, 0)$ at $y = y_{\max}$. When the flow is no longer laminar, the coefficient K_p has to change to a value different from 1 according to eq. (8) above. Using the above formula for the base flow gives the perturbation equations

$$\begin{aligned} \mathbf{u}'_t + \nabla p' - \frac{1}{Re} \nabla^2 \mathbf{u}' + \left(K_p \frac{df}{d\eta} \cdot \nabla \right) \mathbf{u}' \\ + (\mathbf{u}' \cdot \nabla) K_p \frac{df}{d\eta} = -\epsilon \mathbf{u}' \cdot \nabla \mathbf{u}', \end{aligned} \quad (9)$$

$$\nabla \cdot \mathbf{u}' = 0. \quad (10)$$

For the nonlinear approach we have, apart from the solution coefficients $\hat{\mathbf{u}}_{bji}$, three additional unknowns (*e.g.* $c = c_r$, ϵ and K_p) in the system of nonlinear equations. Hence we need to add three additional equations to close the system; two of them set the phase of the solution, *i.e.*

$$\Re \left[\sum_{i=0}^{NY} \hat{v}_{1-1i} T_i(y=3) \right] = 1, \quad (11a)$$

$$\Im \left[\sum_{i=0}^{NY} \hat{v}_{1-1i} T_i(y=3) \right] = 0. \quad (11b)$$

The third equation is eq. (8) for K_p . Reality of the physical solution implies that $\hat{\mathbf{u}}_{bji} = \hat{\mathbf{u}}_{-b-ji}^*$ where $*$ here refers to the complex conjugate, therefore only modes corresponding to $b \geq 0$ need to be considered (and $j \geq 0$ when symmetry is imposed in z), the others are recovered by the complex conjugate. We use a collocation method in y and a Galerkin method in x and z , leading to a set of ordinary differential equations to be solved in y . The Galerkin method has advantageous properties; rather than imposing zero residual on each collocation point the error is minimised in an integral sense over the whole domain (see *e.g.* [75]). For example, in [46] a full Galerkin method in all 3 coordinates had to be used in order to solve properly the Navier-Stokes equations. We use the collocation points γ_k according to the Gauss-Lobatto distribution to discretise the equations in the wall-normal direction

$$\gamma_k = \cos \left(\frac{k\pi}{NY} \right), \quad k = 0, 1, 2, \dots, NY. \quad (12)$$

The equations are solved in the physical domain $0 \leq y \leq y_{\max}$ where a mapping is used and the wall-normal coordinate $-1 \leq \gamma(y) \leq +1$ is transformed as

$$y_k = p \frac{1 + \gamma_k}{q - \gamma_k}. \quad (13)$$

The above dependence between y and γ leads to $du/dy = (du/d\gamma)(d\gamma/dy)$. Furthermore $p = y_i y_{\max} / (y_{\max} - 2y_i)$ and $q = 1 + 2p/y_{\max}$, where y_i and y_{\max} are set to 8 and 40, respectively. This mapping then puts half of the collocation grid points in the domain $0 \leq y \leq y_i$. The energy E' of the wavy part of the flow can be used to measure the amplitude of the solution and is defined as

$$\begin{aligned} E' = \frac{\hat{E}'}{\hat{\rho} \hat{U}_\infty^2 \hat{\delta}_0^3} = \frac{4\epsilon^2 \pi^2}{\alpha \beta} \int_0^{y_{\max}} \sum_{b=1}^{NX} \sum_{j=-NZ}^{NZ} \left[\tilde{u}^{(bj)} \tilde{u}^{*(bj)} \right. \\ \left. + \tilde{v}^{(bj)} \tilde{v}^{*(bj)} + \tilde{w}^{(bj)} \tilde{w}^{*(bj)} \right] dy. \end{aligned} \quad (14)$$

Another way to measure the wave amplitude is to consider a part of the solution spectrum, A_{3D} , where the Fourier indices $(b, j) = (1, 1)$ are assumed to contain the major part of the energy

$$A_{3D} = \sqrt{\epsilon^2 \sum_{i=0}^{NY} |\hat{u}_{11i}|^2 + |\hat{v}_{11i}|^2 + |\hat{w}_{11i}|^2}, \quad (15)$$

with \hat{u}_{11i} being the solution coefficients of eq. (6).

Experiments on turbulence have consistently shown that the mean spanwise spacing $z^+ = \hat{z} \hat{u}_\tau / \hat{v}$ between low speed streaks is around 100 [38, 76, 77] with $\hat{u}_\tau = \sqrt{\hat{\tau}_w / \hat{\rho}}$ the friction velocity. When expressed in terms of the total mean velocity (integrated over x and z) $\bar{u}_m(y)$, the spanwise spacing is

$$z^+ = \frac{2\pi}{\beta} \sqrt{Re \frac{d\bar{u}_m}{dy} \Big|_{y=0}}, \quad (16)$$

where \bar{u}_m is the solely y -dependent part of the total flow, *i.e.* the Blasius flow plus that part of the perturbation being dependent on y only, *i.e.* $\bar{u}_m(y) = K_p f'(\eta) + \epsilon \tilde{u}^{(0,0)}(y)$. Turbulence intensities are measured often and represented by the root-mean-square velocities defined for the u -component as a function of the global coordinate y as

$$u_{\text{rms}}^2(y) = \frac{1}{\lambda_x \lambda_z} \int_0^{2\pi/\alpha} \int_0^{2\pi/\beta} (u - \bar{u}_m)^2 dX dz. \quad (17)$$

The measure of u_{rms} is computed by considering all spatial fluctuations in both X and z . A similar way to measure the turbulence intensity or the amplitude of the fluctuations is to compute the root-mean-square velocities normalised by the friction velocity \hat{u}_τ

$$u_{\text{rms}}^+(y) = \left(\frac{1}{Re} \frac{d\bar{u}_m}{dy} \right)^{-1/2} u_{\text{rms}}(y). \quad (18)$$

The shape factor H is defined as

$$H = \frac{\hat{\delta}_*}{\hat{\theta}} \quad (19)$$

and can be used to determine the state of the boundary layer flow; $\hat{\delta}_* = \int_0^\infty (1 - \hat{u}/\hat{U}_\infty) d\hat{y}$ is the displacement thickness and $\hat{\theta} = \int_0^\infty (\hat{u}/\hat{U}_\infty)(1 - \hat{u}/\hat{U}_\infty) d\hat{y}$ is the momentum thickness. Using the non-dimensionalised velocity we arrive at

$$\hat{\delta}_* = \hat{\delta}_0 \int_0^{y_{\text{max}}} \left(1 - K_p \frac{df}{d\eta} - \epsilon \tilde{u}^{(0,0)}(y) \right) dy, \quad (20)$$

$$\hat{\theta} = \hat{\delta}_0 \int_0^{y_{\text{max}}} \left(K_p \frac{df}{d\eta} + \epsilon \tilde{u}^{(0,0)}(y) \right) \times \left(1 - K_p \frac{df}{d\eta} - \epsilon \tilde{u}^{(0,0)}(y) \right) dy. \quad (21)$$

For laminar flow $H = 2.59$ and for turbulent flow the shape factor equals approximately 1.5. To convert the Reynolds number from the present non-dimensionalised system, to a system scaled by the displacement thickness $\hat{\delta}_*$, one uses the formula $Re_* = (\hat{\delta}_*/\hat{\delta})Re$ or $Re_* \approx 1.7208Re$.

3 Results

3.1 Exact coherent structures

We search for three-dimensional nonlinear exact coherent structures (ECS) having $c = c_r$ (*i.e.* $c_i = 0$, see eq. (6)) with the aim to find solutions that may have relevance to the turbulence transition. The solutions are local since we have assumed a boundary layer flow that is locally parallel. To confirm the code for the linear stability of the parallel Blasius flow the results contained in [12, 28, 68] were reproduced, cf. table 1. Moreover the nonlinear two-dimensional results contained in [66] have been reproduced. Analysing the Navier-Stokes equations and the continuity equation

Table 1. The critical point reproduced using our linear stability code for the Blasius flow. The critical point presented in [28] is $Re_* = 519.4$ and $c = 0.3965$. In the present non-dimensionalised system we arrive at $Re = 301.649$ which translates to $Re_* = 519.074$ which also agrees with results presented in [68] and [12]. For the 3D linear stability we reproduce the eigenvalues contained in [28] on p. 507. Using the nonlinear code for the above parameter values and bringing A_{3D} (see eq. (15)) to zero we arrive at the bifurcation point, a proof of the consistency between the linear and nonlinear codes employed.

α	β	Re	α_*	β_*	Re_*	c
0.17608	0	301.649	0.303	0	519.074	0.39645

one finds that the following reflect symmetry about the line $z = 0$ is admitted:

$$\mathcal{Z} : (u, v, w, p)(x, y, z, t) = (u, v, -w, p)(x, y, -z, t). \quad (22)$$

Considering symmetry \mathcal{Z} and no symmetry in y yields the following expansion:

$$\begin{bmatrix} u' \\ v' \\ w' \\ p' \end{bmatrix} = \sum_{b=0}^{NX} \sum_{j=0}^{NZ} \sum_{i=0}^{NY} \begin{bmatrix} \hat{u}_{bji} T_i(\gamma(y)) \cos j\beta z \\ \hat{v}_{bji} T_i(\gamma(y)) \cos j\beta z \\ \hat{w}_{bji} T_i(\gamma(y)) \sin j\beta z \\ \hat{p}_{bji} T_i(\gamma(y)) \cos j\beta z \end{bmatrix} e^{Ib\alpha(x-ct) + \text{c.c.}}, \quad (23)$$

where c.c. stands for complex conjugate and \hat{u}_{bji} are the unknown solution coefficients. The perturbation \mathbf{u}' in eq. (23) can be decomposed into its steady x -independent part $\tilde{\mathbf{U}}(y, z) = (\tilde{U}, \tilde{V}, \tilde{W})$ (represented by the solution coefficients $\hat{\mathbf{u}}_{0ji}$) and the x -dependent wavy part $\tilde{\mathbf{u}}(x, y, z, t)$, having the solution coefficients $\hat{\mathbf{u}}_{bji}$ with $b \geq 1$. The number of governing equations, *i.e.* the Navier-Stokes equations in their primitive form and the continuity equation (the unknown functions being $\tilde{u}, \tilde{v}, \tilde{w}, \tilde{U}, \tilde{V}$ and \tilde{W}), are reduced following the steps outlined in [78] and [46]. This leads to equations for the x -dependent wavy part $\tilde{\mathbf{u}}$ of the perturbation, *i.e.* the \tilde{v} - and \tilde{w} -component corresponding to the part of the solution of Fourier index $b \geq 1$, see eq. (23). For the x -independent steady part ($b = 0$) of the solution we arrive at equations for the streamwise streaks $\tilde{U}(y, z)$ and the streamfunction $\tilde{\psi}(y, z)$ with solution coefficients referred to as $\hat{\psi}_{0ji}$. The relations between the streamfunction and the rolls (described by \tilde{V} and \tilde{W}) are $\tilde{V}(y, z) = \tilde{\psi}_z(y, z)$ and $\tilde{W}(y, z) = -\tilde{\psi}_y(y, z)$, where the subscripts refer to differentiation with respect to y and z . For the reduced system of equations the unknown functions are $\tilde{v}, \tilde{w}, \tilde{U}$ and $\tilde{\psi}$. The function $\psi(t, y, z)$ is defined as $\psi(t, y, z) = g(t)\tilde{\psi}(y, z)$; then considering the streamwise average (overbar) of eq. (9) and by taking $\mathbf{i} \cdot \nabla \times \overline{(\mathbf{u} \cdot \nabla \mathbf{u})}$ we obtain

$$-\frac{\partial}{\partial t} \nabla^2 \psi = -\frac{1}{Re} \nabla^4 \psi + \mathcal{N}(\psi) + \mathbf{i} \cdot \nabla \times \overline{(\mathbf{u} \cdot \nabla \mathbf{u})}, \quad (24)$$

where \mathcal{N} represents the nonlinear terms of ψ . Since the mean flow averaged over X ($= x - c_r t$) is time-independ-

ent, we look for the solution of the time-independent part $\tilde{\psi}(y, z)$ of ψ . The time derivative in eq. (24) is kept for purposes that will be explained later on. Whether or not the governing equations are in their primitive or reduced form, they can be represented by the vector \mathbf{F} . Then, for solving the equations iteratively, using the Newton-Raphson method, one needs to construct the gradient of \mathbf{F} , in vector form represented by the Jacobian matrix \mathbf{J} . To solve the equations we use the PITCON subroutine, based on a Newton-Raphson technique, developed by Rheinboldt and Burkardt [79, 80], and solves the Navier-Stokes equations iteratively $n = 0, \dots, N$ as shown below (cf. eq. (25)). When mapping out nonlinear solutions in the continuation parameter Ω the algorithm takes the previous converged solution at $\Omega - \Delta\Omega$ as an initial guess, steps forward in Ω and restarts the iteration procedure as follows:

$$-\mathbf{F}(\mathbf{x}^{(n)}; \Omega) = \mathbf{J}(\mathbf{x}^{(n)}; \Omega) \cdot d\mathbf{x}^{(n)}. \quad (25)$$

The solution coefficients $\hat{\mathbf{u}}_{bji}$ in eq. (23) as well as the unknown eigenvalues c_r, ϵ and K_p make up the total number of unknowns $\mathbf{x}^{(n)} = [\hat{\mathbf{u}}_{bji}, c_r, \epsilon, K_p]$ in each iteration and are updated at each step by $\mathbf{x}^{(n+1)} = \mathbf{x}^{(n)} + d\mathbf{x}^{(n)}$ until convergence is reached. When continuing in, e.g. the Reynolds number Re , the vector $\mathbf{F} = \mathbf{F}(\hat{\mathbf{u}}_{bji}, c_r, \epsilon, K_p; Re) = \{F_m\}_{m=1}^{NVAR}$, with $\mathbf{J} = \sum_{k=1}^{NVAR} \partial F_m / \partial x_k$ ($m = 1, \dots, NVAR$) is the Jacobian matrix where $\mathbf{x} = \{x_k\}_{k=1}^{NVAR}$. The reduced system of equations discussed above is preferable rather than using the Navier-Stokes equations in their primitive form. First, because the unknown pressure is eliminated, and second in terms of memory needed to store the Jacobian matrix \mathbf{J} in 64 bits double precision floating-point format (see eq. (25)). For the reduced system, solving for the functions $\check{v}, \check{w}, \check{U}$ and $\check{\psi}$, and a truncation of say $(NX, NY, NZ) = (4, 100, 10)$ the \mathbf{J} has about 22000 columns and thus $22000^2 = 4.84 \times 10^8$ entries in total, corresponding to about 3.6 GB of memory storage for \mathbf{J} . When representing the governing equations in their primitive form, thus solving for the functions $\check{u}, \check{v}, \check{w}, \check{U}, \check{V}$ and \check{W} , using the same truncation as above would require about 1.94×10^9 entries and occupy about 14.5 GB of memory.

3.1.1 Search for ECS bifurcating from the Blasius flow

As a first attempt to discover nonlinear states, solution curves were mapped out in parameter space representing nonlinear three-dimensional finite amplitude waves bifurcating directly from the laminar Blasius flow. As an initial guess PITCON was supplied with the linear eigenmodes of the stability analysis of the Blasius flow shown in fig. 2. The nonlinear solutions computed turned out to possess quite large values of the mean spanwise spacing z^+ (> 600), thus making them of little relevance since z^+ should stay close to 100 according to experimental observations. Checking the solution coefficients closely it was observed that they possessed a chess-board pattern which

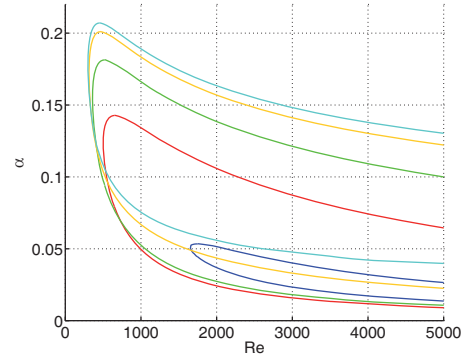


Fig. 2. The stability of the Blasius flow. The figure shows neutral curves ($c_i = 0$) mapped out in $\alpha-Re$ space of selected perturbations of spanwise wave numbers $\beta = 0 - 0.20$ indicated in the figure, where $\beta = 0$ (the turquoise curve), $\beta = 0.05$ (yellow), $\beta = 0.10$ (green), $\beta = 0.15$ (red) and $\beta = 0.20$ (blue). By increasing β the envelope of the linearly unstable solutions is narrowed and pushed towards large Re , making it difficult to find solutions for $\beta > 0.20$.

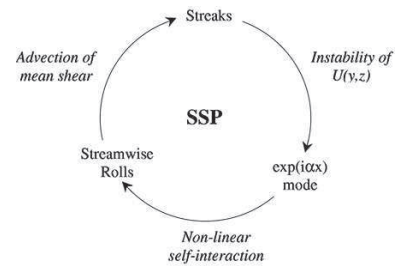


Fig. 3. The self-sustaining process according to [39].

alternated between zero and non-zero values of the $\hat{\mathbf{u}}_{bji}$ in eq. (23). A similar behaviour has also been reported in [70, 81] and [82]. This approach has not been pursued further.

3.1.2 Search for ECS using the self-sustaining process

The self-sustaining process (SSP) allows us to set arbitrary values of β . The main idea of the SSP is shown in fig. 3; it is used to locate approximate solutions to the Navier-Stokes equations. Each step is linear and constructs and partly fills up the full spectrum of coefficients (i.e. the $\hat{\mathbf{u}}_{bji}$) of eq. (23). The flow components contained in the SSP are the streamwise independent rolls of order Re^{-1} here represented by the streamfunction $\psi_{ssp}^{(n)}(t, y, z) = \tilde{\psi}_{ssp}^{(n)}(y, z)e^{\lambda t/Re}$ defined by solving the completely linearised eq. (24) (λ being the growth rate, e.g. $n = 1$ is the least stable mode). The remaining flow structures are the streamwise streaks $\tilde{U}_{ssp}(y, z)$ of order $O(1)$ and neutral linear waves (i.e. $c = c_r$) $\tilde{\mathbf{u}}_{ssp}(x, y, z, t)$ of order $O(Re^{-1})$. Putting together the flow components makes up an approximate weakly nonlinear solution and shows more or less where in parameter space the ECS is located. The fully nonlinear solution is discovered by con-

verting the SSP into a continuation procedure involving a forcing function $\mathbf{f}(y, z)$ [42, 43, 46, 55, 78], *i.e.*

$$\begin{aligned} \mathbf{F} = & \mathbf{u}'_t + \nabla p' - \frac{1}{Re} \nabla^2 \mathbf{u}' + \left(K_p \frac{df}{d\eta} \cdot \nabla \right) \mathbf{u}' \\ & + (\mathbf{u}' \cdot \nabla) K_p \frac{df}{d\eta} + \epsilon \mathbf{u}' \cdot \nabla \mathbf{u}' - \mathbf{f} = \mathbf{0}. \end{aligned} \quad (26)$$

For the case of the Navier-Stokes equations in primitive variables, the \mathbf{f} comes into play in the v -momentum and the w -momentum: $\mathbf{f} = f_v(y, z)\mathbf{j} + f_w(y, z)\mathbf{k}$. In the present case the $\mathbf{f}(y, z)$ is used to force x -independent streamwise rolls, initially in the absence of the nonlinear interactions of the wavy part $\tilde{\mathbf{u}}$ (see eq. (24)). In the reduced system being solved the forcing replaces the left-hand side of eq. (24) and is set equal to $f_A f_\psi(y, z)$ (its analytical form yet to be determined with amplitude f_A). The underlying idea is that we want to replace the term on the left hand side of eq. (24) by the forcing. In order to appreciate the replacement of the $\nabla^2 \psi_t$ -term by the forcing we imagine the fully linearised version of eq. (24) where the forcing is supposed to take the place of the left hand side. We assume the solution $\psi = \tilde{\psi}(y, z)e^{\lambda t/Re}$ (λ being an eigenvalue), arriving at $\lambda \nabla^2 \tilde{\psi}(y, z) = \nabla^4 \tilde{\psi}(y, z)$. The forcing $f_\psi(y, z)$ is then set equal to the term $\nabla^2 \tilde{\psi}(y, z)$ and inserted into the left-hand side of eq. (24) with the purpose of acting as a forcing of the unknown functions on the right hand side. Setting an amplitude f_A on $f_\psi(y, z)$ and marching from low to higher values of f_A we generate solutions of different amplitudes. The idea is to drive particular three-dimensional nonlinear structures with possible similarity to the flow structures observed in [38] or, in this study, the edge state solution shown in fig. 6 of Biau [25]. The solution of Biau resembles very much already known nonlinear solutions such as the flow states on the edge of [83] for the flow in a square duct, or the travelling wave discovered by Okino and Nagata [84] for the same flow case, as well as that of [55] in the circular pipe flow. To carry out an operation of driving particular solutions an analytical streamfunction is constructed guided by the velocity field shown in fig. 6 of [25], and then used for defining the forcing. The first step is to use the continuity equation to determine a suitable function for the x -independent rolls $\tilde{\mathbf{V}}(y, z) = \tilde{V}(y, z)\mathbf{j} + \tilde{W}(y, z)\mathbf{k}$, which satisfies the no-slip boundary conditions at $y = 0$ and the asymptotic conditions at $y = y_{\max}$. Then, using the given relation between $\tilde{\psi}(y, z)$, $\tilde{V}(y, z)$ and $\tilde{W}(y, z)$ we can define the streamfunction as

$$\tilde{\psi}(y, z) = -\Im m \left(y^2 \cos(b_2 y) e^{-\beta y} e^{i\beta z} \right). \quad (27)$$

We choose a cosine expression to define the dependence in y where the constant b_2 determines its periodicity. Whether or not different values of b_2 lead to different limit states has not been tested; in this study we have set $b_2 = 0.5$. In order to satisfy both the Neumann and the Dirichlet boundary conditions at $y = 0$ the term y^2 is used; the exponential $e^{-\beta y}$ sets the correct asymptotic decay in the free-stream (see the discussion below eq. (6)). Finally,

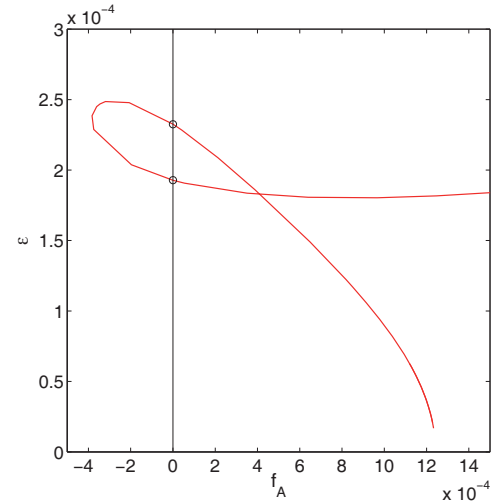


Fig. 4. Continuation in f_A from a finite value to the points where $f_A = 0$ for $(\alpha, \beta, Re, b_2) = (0.20, 0.45, 400, 0.5)$ and truncation $(NX, NY, NZ) = (3, 80, 10)$. The vertical axis ϵ measures the amplitude of the perturbation defined in the sentence above eq. (4).

in order to accord with the imposed symmetry in eqs. (22) and (23), we consider the imaginary part of the imposed periodicity in z . Then, eq. (27) is used for representing $f_A \nabla^2 \tilde{\psi}$ which replaces the left-hand side of eq. (24) for forcing the nonlinear solutions. Again the PITCON subroutine is used for finding the nonlinear solutions. We need an initial guess to initiate the iterations that finally lead to a converged nonlinear solution. The initial guess is found in three steps in which the nonlinear interactions of the wavy part $\tilde{\mathbf{u}}$ are always neglected. First we force nonlinear $\tilde{\psi}(y, z)$ by $f_A f_\psi(y, z)$ as already explained above, with the one difference that we now include the $\mathcal{N}(\tilde{\psi})$ -terms. This step gives us a solution for the rolls $(0, \tilde{V}(y, z), \tilde{W}(y, z))$. Then the rolls (represented by the streamfunction $\tilde{\psi}$), in turn drive a x -independent streamwise flow $\tilde{U}(y, z)$ which is superimposed on the Blasius flow for defining a new base flow together with $\tilde{\psi}(y, z)$. Performing a linear stability analysis of the new base flow, and locating a neutrally stable eigenmode $c_i = 0$ at a certain combination of the parameters $(f_A, Re, \alpha, \beta, b_2, \epsilon)$, yields the starting point necessary for embarking on the fully nonlinear approach, using the PITCON subroutine. Having found the point where the forcing amplitude $f_A = 0$, access is given to the parameter space of the relevant system of equations without the forcing. Figure 4 shows how f_A is gradually brought to zero by resolving eqs. (26), pointing out two unforced nonlinear solutions at $f_A = 0$. In order to get an idea of the convergence of the two unforced solutions in fig. 4 the decay of the energy in each combination of the Fourier components b, j is shown in fig. 5. For a fixed Fourier index b one sees a decay of up to 10 orders of magnitude when comparing $E_{b,j=0}$ and $E_{b,j=NZ}$. Furthermore, the energy contribution from the last mode in x , *i.e.* for $b = 3 = NX$, is nearly negligible compared to that from the $b = 1$ -mode. The value of the phase speed c_r converges

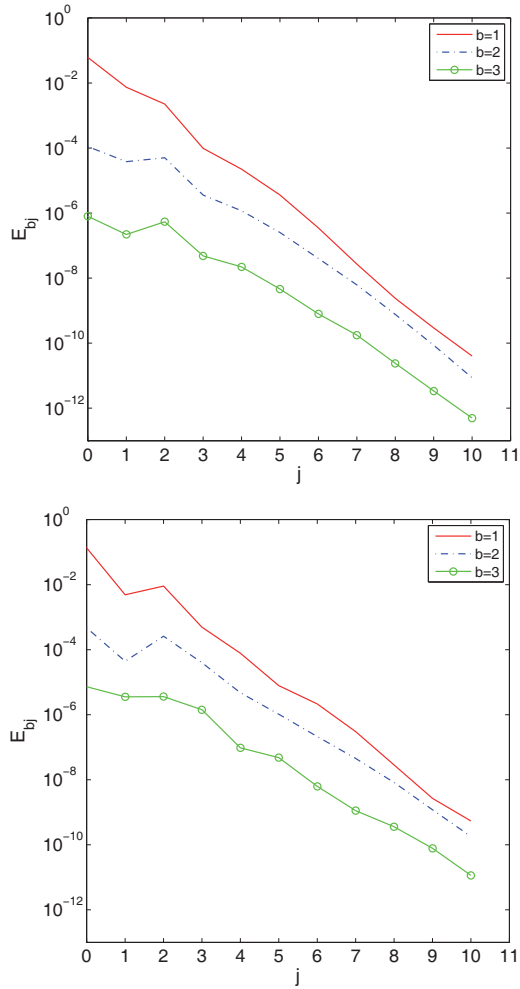


Fig. 5. The decay of the energy content E_{bj} of each combination of the Fourier modes (b, j) of the wavy part of the perturbation, for $b = 1, 2, 3$ ($= NX$) and $j = 0, 1, \dots, 10$ ($= NZ$). The solutions correspond to the $f_A = 0$ situation (black circles) in fig. 4, the *upper* plot shows the lower solution and the *bottom* plot the upper solution. There is a decay of about 8 orders of magnitude comparing $E_{b,0}$ and $E_{b,NZ}$, indicating convergence.

quickly for the lower solution in fig. 4, for a truncation of $(NX, NY, NZ) = (3, 120, 10)$ we have $c_r = 0.3934$ and comparing with a very low truncation $(1, 80, 5)$ the difference in c_r is only of order 10^{-4} , thus giving confidence that the used truncation is sufficient. A more extensive analysis on the convergence of the solutions is shown later on in fig. 9. The mean streamwise velocity field of the two unforced solutions are shown in fig. 6 and can be used to distinguish the solutions from each other when changing, *e.g.* α or β . The feature of the two velocity fields shown might appear as essentially the same but the velocity components have different amplitudes, as indicated in the same figure. As mentioned earlier, the velocity field of the edge state solution shown in fig. 6 of [25] has been used as a target state for finding TWS in the present nonlinear study. The solution of [25] is a snapshot in time and the underlying thought behind using it as a target state is

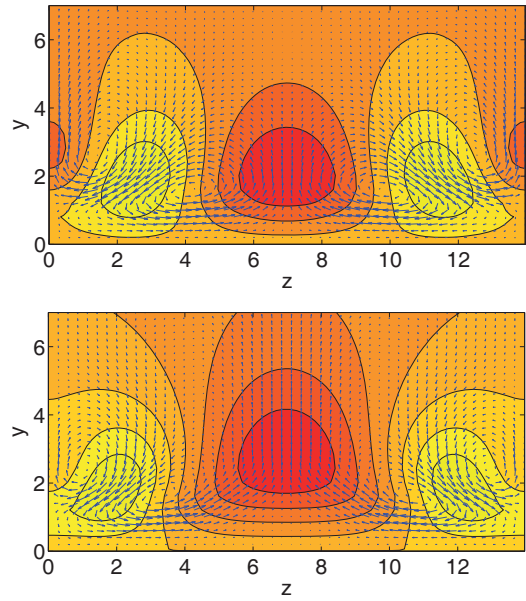


Fig. 6. The velocity field (averaged over x) of the two unforced solutions shown in fig. 4 at $f_A = 0$ (black circles). The contour levels represent the streamwise velocity u and range between $\min(u)$ and $\max(u)$ in steps of 0.017, and the arrows show the cross-stream velocity components. The color coding goes from most negative (dark) to most positive (light). Top: the lower solution having $(\min(u), \max(u)) = (-0.0620, 0.0394)$, $(\min(v), \max(v)) = (-7.30 \cdot 10^{-4}, 8.32 \cdot 10^{-4})$ and $(\min(w), \max(w)) = (-0.0011, 0.0011)$. Bottom: the upper solution of higher amplitude having $\min(u) = -0.0851$ and $\max(u) = 0.0488$, $(\min(v), \max(v)) = (-8.54 \cdot 10^{-4}, 6.92 \cdot 10^{-4})$ and $(\min(w), \max(w)) = (-0.0014, 0.0014)$. Both figures show the mean flow in the shape of a four-vortex structure near the wall.

to look into the relevance of the converged nonlinear travelling wave solution to the time-dependent orbit of Biau. That is, would the TWS be embedded in the same state space traced out by the edge state? In [25] one finds a streamwise averaged flow field having in total 4 vortices, with two vortices on each side of the center of the flow domain, near the plate and aligned on top of each other diagonally in the wall-normal direction. This is similar to what is shown in fig. 6 of the present study, giving some confidence that the TWS is at least near the solution of Biau. In the same figure we see the presence of vortices associated with low and high speed streaks generated by the lift-up process. In both Biau and the present study the more energetic part of the velocity field is situated next to the wall and inside the boundary layer, $y < 5$. The full velocity field of the perturbation (still at $f_A = 0$) with all modes in x included is shown in figs. 7 and 8, presenting the x -variation of the solutions. The upper solution has a larger amplitude as can be seen from *e.g.* the absolute values of $\min(u)$ and $\max(u)$ given in the caption. The figures show a low-speed streak sandwiched between two high-speed streaks near the wall. At this Reynolds number the most energetic structure is the low speed streak in the centre of the flow domain. A noticeable change with the

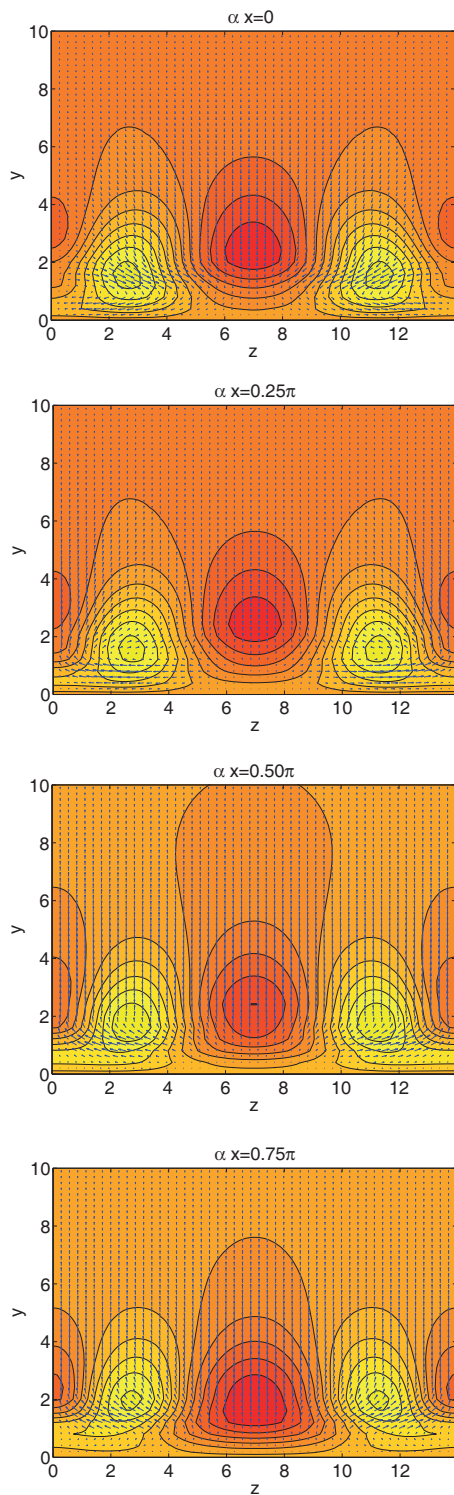


Fig. 7. The full perturbation velocity field of the *lower* unforced solution of fig. 4. The figure represents 4 values of coordinate x whose values are indicated at the top of each figure. The contour levels represent the streamwise velocity u and range between $(\min(u), \max(u)) = (-0.0651, 0.0492)$ of the 4 values of x in steps of 0.01, and the arrows show the cross-stream velocity components. The color coding goes from most negative (dark) to most positive (light). The range in v and w are: $(\min(v), \max(v)) = (-0.0023, 0.0066)$ and $(\min(w), \max(w)) = (-0.0085, 0.0085)$.

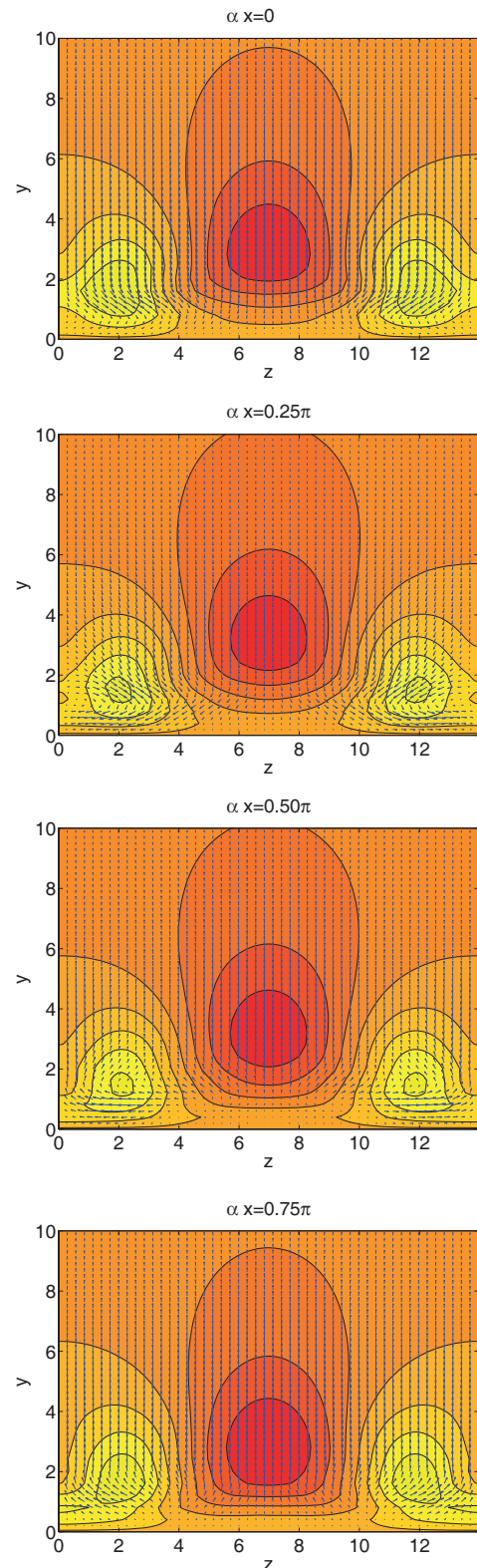


Fig. 8. The full perturbation velocity field of the *upper* unforced solution of fig. 4. The contour levels represent the streamwise velocity u and range between $(\min(u), \max(u)) = (-0.0830, 0.0612)$ of the 4 values of x in steps of 0.0175, and the arrows the cross-stream velocity components. The color coding goes from most negative (dark) to most positive (light). The range in v and w are: $(\min(v), \max(v)) = (-0.0073, 0.0095)$ and $(\min(w), \max(w)) = (-0.0074, 0.0074)$.

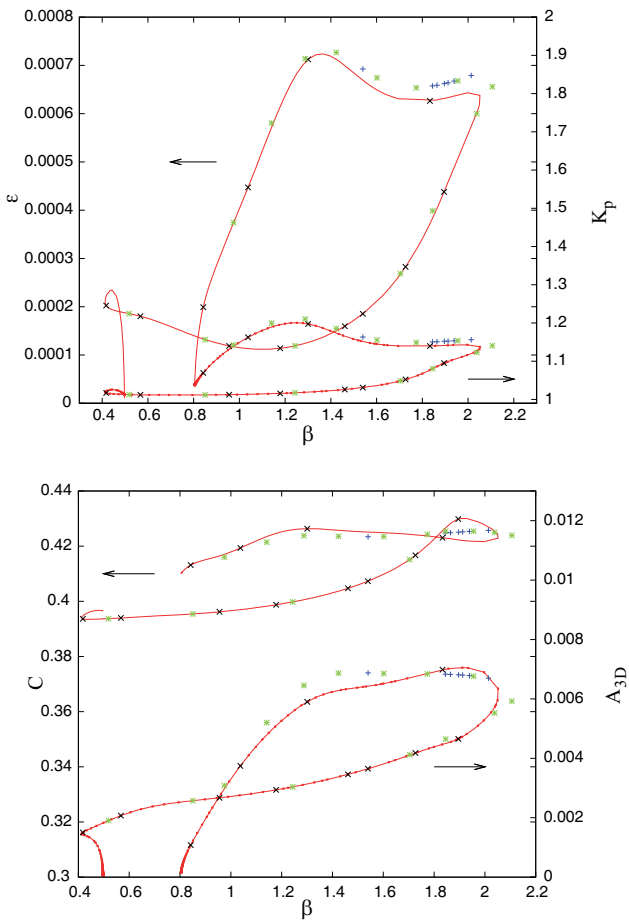


Fig. 9. Envelope in β of the nonlinear solutions for $(\alpha, Re, b_2) = (0.20, 400, 0.5)$ as function of ϵ and K_p (top) and as function of $c = c_r$ and A_{3D} (bottom). The arrows point out to which vertical axis the curves belong. To demonstrate convergence, solutions of different truncations are shown: red solid curve and red solid-dotted curve correspond to $(NX, NY, NZ) = (4, 100, 5)$, black \times $(4, 120, 10)$, green $*$ $(8, 120, 5)$. The blue $+$ $(10, 120, 5)$ are added to show convergence on the upper branch. As the figure shows, the value of K_p sits in the interval $1 < K_p \leq 1.20$. Even though the results of [68] for the Blasius boundary layer accounts only for $\beta = 0$ at a slightly larger Re the wave speed c is close to those indicated here.

streamwise distance x is the swirling motion of the vortices near the z -boundaries of the periodic cell between $y = 0$ and 3. Here one sees the rolls moving slightly back and forth in the spanwise direction as we proceed downstream. The motion within that region corresponds also to the more pronounced flow structure of the whole velocity field (cf. fig. 6).

Having found a solution to the unforced system ($f_A = 0$) at $Re = 400$ allows for an exploration of the parameter space in α , β and Re . The perturbation equations (9) governing the boundary layer flow admit any spanwise wave number β as opposed to *e.g.* the circular pipe flow that only takes integer values. To map out the relevant solutions in parameter space one can use any of the two unforced solutions in fig. 4. Figure 9 shows the envelope

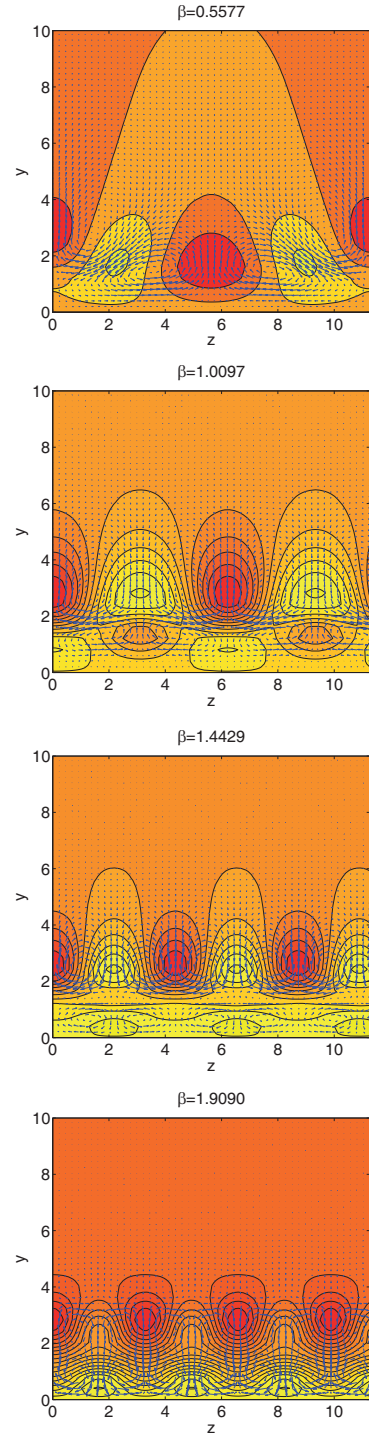


Fig. 10. The mean velocity field of the perturbation with symmetry Z for $\alpha = 0.20$, $Re = 400$ for the following values of β : 0.5577, 1.0097, 1.4429 and 1.9090. All 4 solutions correspond to a base flow with K_p ranging between 1.012 and 1.097 and truncation $(NX, NY, NZ) = (8, 120, 5)$. The range in z of each velocity field corresponds to the wavelength of $\beta = 0.5577$ in order to show the same spanwise domain. The contour levels represent the streamwise velocity u and range between $(\min(u), \max(u))$ of each solution with a step of 0.017, 0.004, 0.005 and 0.008 between the contour levels according to the order given above in β ; the arrows are the cross-stream velocity components. The color coding goes from most negative (dark) to most positive (light). Properties of the solutions are given in table 2.

Table 2. Properties of the 4 solutions in β shown in fig. 10 for symmetry Z , $(\alpha, Re) = (0.20, 400)$ and $(NX, NY, NZ) = (8, 120, 5)$. The value of H for the laminar Blasius flow is 2.59. The shown values of c are similar to those presented in the study of [68].

β	c	z^+	H	K_p
0.5577	0.3939	131	2.5845	1.012
1.0097	0.3967	72	2.5848	1.013
1.4429	0.4042	51	2.5761	1.025
1.9090	0.4273	40	2.5321	1.097

in β of the solutions for $Re = 400$ and $\alpha = 0.20$. The critical Re and α where Tollmien-Schlichting waves start to amplify is approximately 302 and 0.18. Beyond that point the flow is known to gradually develop a spanwise (z) dependence in the course of transition. Therefore, to look into various z -dependent solutions and to get an impression on how they change with the spanwise wave number β we fix $Re = 400$ and $\alpha = 0.20$ and pick 4 values of β from fig. 9. The chosen solutions are situated along the lower branch in the same figure, *i.e.* that part of the curve where $K_p \approx 1$ and are shown in fig. 10, presenting the mean flow field (averaged over x) of the perturbation. The mean is shown in order to distinguish the solutions with different β 's. Along the same branch (the lower) in fig. 9 the value of z^+ varies between 130 for the lower β to 40 for the larger value. The value $z^+ = 100$ characteristic of turbulent flows is recovered for $\beta \approx 0.728$. In fig. 11 the variation of z^+ with β is extracted from the entire envelope of the solution curve shown in fig. 9, and for two additional values of α . The curves for $\alpha = 0.16$ and 0.20 are almost overlapping, at $(\alpha, \beta) = (0.20, 0.728)$ and $(\alpha, \beta) = (0.16, 0.733)$ we have $z^+ = 100$, while for $\alpha = 0.33$ the band of β 's forms a closed loop and $z^+ < 100$ for all β . Figures 12-14 show the corresponding Fourier components of the first x -dependent mode ($b = 1$) for $(\alpha, \beta, z^+) = (0.20, 0.728, 100)$ and $(0.16, 0.733, 100)$. The case $(\alpha, \beta, z^+) = (0.33, 1.440, 67)$ is also included even though its spanwise spacing seems too low to be relevant for transition (at least on the basis of the spanwise spacing of the near-wall structures). The thickness of the laminar Blasius boundary layer corresponds to $y = 5$ and the figure clearly shows that the Fourier modes are situated within that distance, apart from the $j = 0$ component that decays slower with y than the other modes. All three solutions have values of c between 0.38 and 0.46, to be compared to the value of a Tollmien-Schlichting wave at the critical point of linear instability where $c \approx 0.40$.

The two solutions at $(\alpha, \beta) = (0.20, 0.728)$ and $(\alpha, \beta) = (0.16, 0.733)$ correspond both to a spanwise spacing of 100. In terms of wall units in the normal direction $y^+ = \hat{y}\hat{u}_\tau/\hat{v}$, considering the same two solutions above, the main contribution from the cross-flow and the streamwise flow lies within the domain $0 \leq y \leq 3$, which translates to $0 \leq y^+ \leq 35$. Thus, the ECS, if embedded in a turbulent boundary layer, would be contained within the buffer layer.

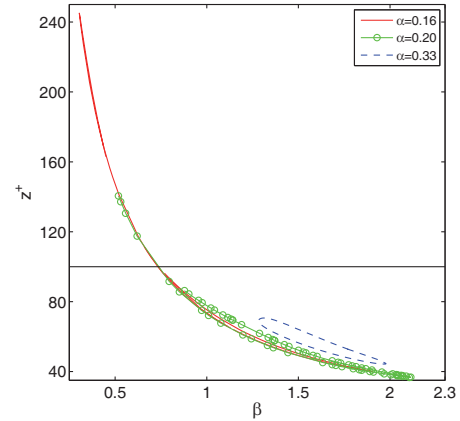


Fig. 11. Variation of z^+ as a function of β for symmetry Z at $Re = 400$ and $\alpha = 0.16, 0.20$ and 0.33 . The horizontal line corresponds to $z^+ = 100$.

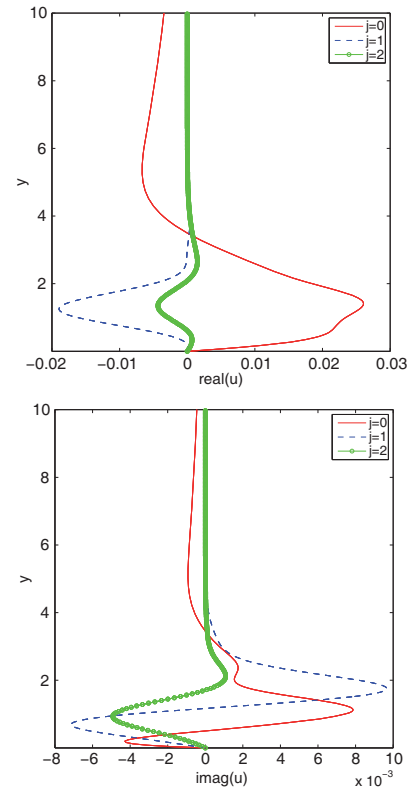


Fig. 12. Fourier components of u (real and imaginary multiplied by ϵ) of the nonlinear solution with $z^+ = 100$ for $(\alpha, \beta, Re) = (0.16, 0.733, 400)$. The truncation used is $(NX, NY, NZ) = (8, 120, 8)$; it is more than adequate and corresponds to around 39000 unknowns, real and imaginary for \hat{u}_{bji} . The value of H is 2.578 and $c = 0.384$. The selected Fourier modes correspond to $b = 1$ and $j = 0, 1$ and 2 , as pointed out by the legends.

Search for travelling waves on the edge of chaos

Using any of the two unforced nonlinear solutions at $f_A = 0$ in fig. 4 as an initial guess we can map out solutions in parameter space. To continue the comparison to the time-dependent dynamics of the separatrix in [25]

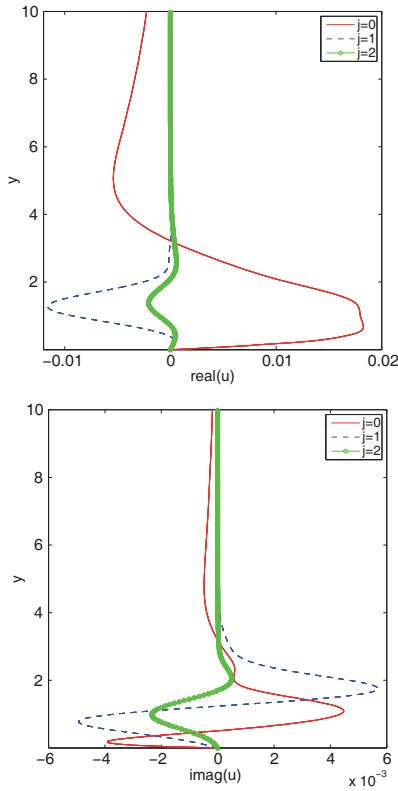


Fig. 13. Fourier components of u (real and imaginary multiplied by ϵ) of the nonlinear solution having $z^+ = 100$ for $(\alpha, \beta, Re) = (0.20, 0.728, 400)$. The truncation used is $(NX, NY, NZ) = (8, 120, 8)$. The value of H is 2.588 and $c = 0.395$. The selected Fourier modes correspond to $b=1$ and $j=0, 1$ and 2, as pointed out by the legends.

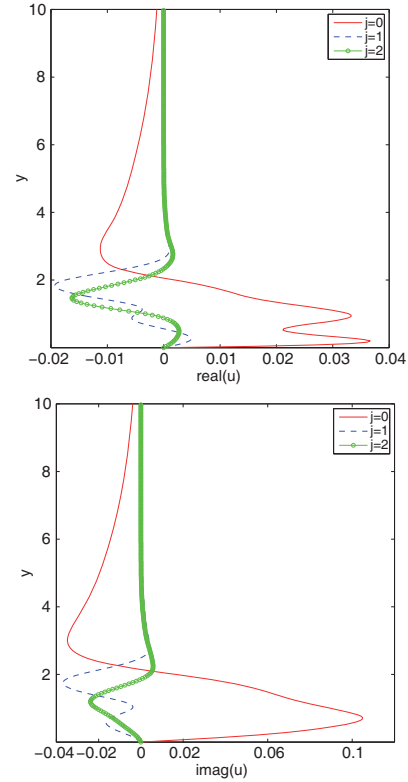


Fig. 14. Fourier components of u (real and imaginary multiplied by ϵ) of the nonlinear solution having $z^+ = 67$ for $(\alpha, \beta, Re) = (0.33, 1.440, 400)$. The truncation used is $(NX, NY, NZ) = (8, 120, 8)$. The value of H is 2.534 and $c = 0.463$. The selected Fourier modes correspond to $b = 1$ and $j = 0, 1$ and 2, as pointed out by the legends.

the travelling wave solutions of the present study were mapped out in Re , α and β until a solution corresponding to $z^+ = 100$ was found. The parameter values used in [25], based on the displacement thickness are $Re_* = 1000$ with a period in the streamwise and spanwise directions equal to $L_x^* = 17.5$ and $L_z^* = 10$. This translates to $Re = 581$, $\alpha = 0.209$ and $\beta = 0.365$ in the present non-dimensional system. At this Re the maximum amplitude of the fluctuations of the edge state solution computed by [25] is $\max[u_{rms}] = 0.09$, fairly close to the reported turbulent value of 0.13. At the same time one needs to take into account the fact that the flow is still very close to the laminar state. Having found a solution at $Re = 581$ and $z^+ = 100$, the ECS were mapped out in α and β to search for ECS with a possible connection to the solution reported in [25]. The two extreme points of the curve mapped out in the α - β -system correspond to $\epsilon \rightarrow 0$, where ϵ is the amplitude presented in connection with eq. (4).

The closest we managed to get to the solution of [25] is $(Re, \alpha, \beta) = (581, 0.195, 0.890)$ using a truncation of $(NX, NY, NZ) = (6, 100, 5)$, which is the point where the solutions start to bundle up at the extreme point of the curve mapped out in α and β . In the scalings of [25] this corresponds to a streamwise length of $L_x^* = 18.8$ and a spanwise length of $L_z^* = 4.1$. The shape factor H of the

TWS at these parameter values is 2.57 whereas for the results in [25] a periodic limit cycle is observed having $2.34 \leq H(t) \leq 2.56$, indicating that both flow states are fairly close to the laminar state, for which $H = 2.59$. Other values to characterise this particular solution are $\epsilon \approx 2.8 \cdot 10^{-5}$, the speed of the wave $c = 0.387$; the amplitude of the mean flow integrated over x of the perturbation $|\bar{u}^x| = 0.068$ and $|\bar{v}^x| = 0.00093$, where $\bar{v}^x = \bar{v}^x \mathbf{j} + \bar{w}^x \mathbf{k}$, giving a ratio of the amplitude of the streamwise flow to the vortices $|\bar{u}^x|/|\bar{v}^x|$ of 73, *i.e.* a streak-dominated flow. In [25] it is reported that $\max[u_{rms}] = 0.09$, whereas the fluctuation amplitude of the TWS corresponds to approximately 0.04 (see eq. (17)). The $\max[u_{rms}]$ of the TWS is low since we consider a solution where $\epsilon \rightarrow 0$. On the same curve, the solution having the largest amplitude of $u_{rms}(y)$ reaches up to 0.06, but corresponds to a wave of longer streamwise wave length. The conclusion is that the TWS and the edge state solution have similar mean streamwise spacing z^+ (assumed), a good match of the wave length in x but in the spanwise direction z the edge state has a wave length that is longer than that of the travelling wave, and the amplitude of $u_{rms}(y)$ in [25] is larger. In terms of the shape factor it seems that the trajectory on the separatrix makes short-time visits to the values of the travelling wave, but the fact that they have different spanwise

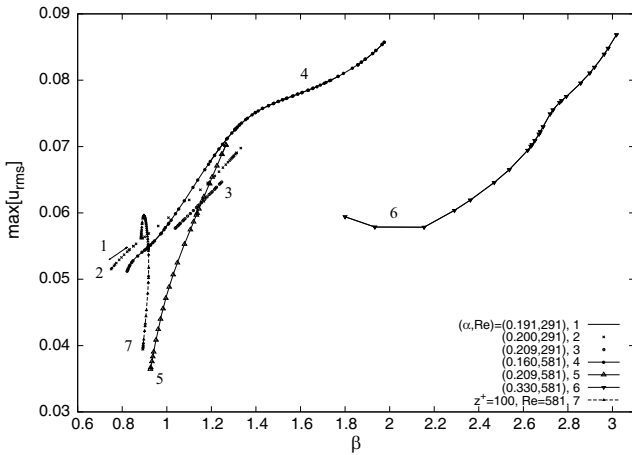


Fig. 15. $\text{Max}[u_{\text{rms}}]$ as function of β for $\alpha = 0.16, 0.209$ and 0.33 , plus the case $z^+ = 100$, at $Re = 581$, and represented by curves 4-7. For the solutions discovered the restriction $K_p \leq 1.30$ is imposed in order to put focus on solutions considered more relevant, and is imposed on curves 5 ($1.031 \leq K_p \leq 1.30$) and 6 ($1.277 \leq K_p \leq 1.30$). The interval in K_p of the remaining curves is 1.066 - 1.181 (curve 4) and 1.022 - 1.108 (curve 7). The target value is that computed by [25], *i.e.* $\text{max}[u_{\text{rms}}] = 0.09$ for $\alpha = 0.209$ and $\beta = 0.365$. Curve 4 and 6 almost make it to that point having $\text{max}[u_{\text{rms}}] = 0.086$ and 0.087 respectively. The TWS of the same α as Biau only reaches as far as 0.07 . For $Re = 291$ all solution curves stay in the interval $1.025 < K_p \leq 1.047$. For this case the target value of $\text{max}[u_{\text{rms}}]$ is 0.12 , computed by [25], and is not reached by any of the TWS considered with the following values of α : $0.191, 0.200$ and 0.209 . The closest to that of Biau is 0.07 for $\alpha = 0.200$ and $\beta = 1.332$, see curve 2. For $Re = 291$ the $\text{max}[u_{\text{rms}}]$ falls into the same region as the nonlinear Tollmien-Schlichting waves computed by [68] of the Blasius boundary layer, although therein $\beta = 0$.

periodicity renders the match not completely convincing. Since the edge state solution is situated close to the laminar flow it is not evident that z^+ should equal 100 . To get an idea of the dependence of $\text{max}[u_{\text{rms}}]$ on α and β (keeping $Re = 581$) we remove the restriction on z^+ with the hope of bringing the TWS closer to the point in parameter space where the edge state of [25] is situated. In this case a larger part of the parameter space is available and we can thus bring the TWS to $\alpha = 0.209$ which gives us the aimed value of the streamwise length of the perturbation. Considering $\alpha = 0.16, 0.209$ and 0.33 and mapping out the solutions in β we find that it is still not possible to let the TWS survive at β 's as low as 0.365 , which defines the spanwise domain set in the study of Biau. For the same α 's the minimum values of β are $0.81, 0.92$ and 1.38 . Since, for certain cases, the value of K_p can become too large (> 2 , where $K_p = 1$ for the laminar flow) we consider only fairly low values, or $K_p \leq 1.30$. Figure 15 presents the envelope of β showing values of the $\text{max}[u_{\text{rms}}]$ for the 3 chosen values of α , and the case $z^+ = 100$ (for which also α changes along the shown branch). The case $Re = 291$ is also presented in the same figure, but will be discussed later on. For $(\alpha, \beta) = (0.16, 1.98)$ and $(\alpha, \beta) = (0.33, 3.02)$ at

Table 3. Properties of a selection of the travelling wave solutions (top 4 rows) shown in fig. 15 compared to the time-dependent edge state solution of [25] (bottom row), all at $Re = 581$. The u_{rms} refers to its maximum value. The wave speed c of the TWS is, in the order of appearance from top to the fourth row: $0.387, 0.399, 0.390$ and 0.469 . The values shown of the travelling wave solutions are those that are the closest to the $\text{max}[u_{\text{rms}}]$ computed by [25] (row 2 and 4) and has the turbulent value $z^+ = 100$ imposed (1st row), or has the same value of α (row 3) as the edge state solution of Biau.

α	β	u_{rms}	K_p	z^+	ϵ	H
0.195	0.890	0.039	1.039	100	$2.8 \cdot 10^{-5}$	2.57
0.160	1.976	0.086	1.181	48	$5.3 \cdot 10^{-4}$	2.47
0.209	1.265	0.070	1.299	79	$4.0 \cdot 10^{-4}$	2.50
0.330	3.018	0.087	1.296	33	$1.2 \cdot 10^{-3}$	2.50
0.209	0.365	0.090	N/A	N/A	N/A	2.34-2.56

$Re = 581$ the target value of $\text{max}[u_{\text{rms}}] = 0.09$ computed by [25] is practically reached, having $\text{max}[u_{\text{rms}}] = 0.086$ and 0.087 , but had to be terminated at these points in parameter space due to less convincing convergence for the first case and K_p being larger than 1.30 for the second parameter combination. The velocity field averaged over x of Biau is not known for this Re , the solution of $\alpha = 0.33$ is a rather feature-less 4-vortex flow not showing any characteristic isolated patches of high- and low speed streaks lying side-by-side near the wall, while the solution at $\alpha = 0.16$ is a more interesting 6-vortex flow with K_p reasonably low ($= 1.181$), but still does not show any characteristic streamwise flow structures next to the plate. The solution having exactly the same value of α as Biau ($= 0.209$) displays a velocity field with 8 vortices, with the flow dominated by low-speed streaks situated at both extremes of the spanwise domain. For this Re none of the TWS can be brought down to the same spanwise wave number as Biau. Table 3 presents a compilation of the 3 solutions discussed above at $Re = 581$ together with the results of [25]. A second solution is also presented in [25] at $Re_* = 500$ with a period in the streamwise and spanwise directions equal to $L_x^* = 30$ and $L_z^* = 10$, which translates to $Re = 291$, $\alpha = 0.122$ and $\beta = 0.365$ in our non-dimensionalised system. Judging from fig. 4 therein the time-dependence of the shape factor H seems rather chaotic for $L_x^* = 30$. A periodic solution is also computed in [25] at the same Re and β , but for $L_x^* = 17.5$, equaling $\alpha = 0.209$. The shape factor of the periodic orbit is $2.26 \leq H(t) \leq 2.49$. For the symmetry imposed in this study we were not able to bring the ECS down to $Re = 291$ keeping $z^+ = 100$. A way to improve the match is to simply remove the restriction $z^+ = 100$, doing this, and using as a starting point the very first solution discovered at $(\alpha, \beta, Re) = (0.20, 0.45, 400)$, see fig. 6, we manage to continue the solution down to $Re = 291$ for $\beta = 0.85$. Having found this point in parameter space we proceed by mapping out the solutions in β for $Re = 291$ and $\alpha = 0.20$ fixed, finding the envelope in β ($0.747 \leq \beta \leq 1.335$) shown in fig. 16. As is evident from the figure the value of β is

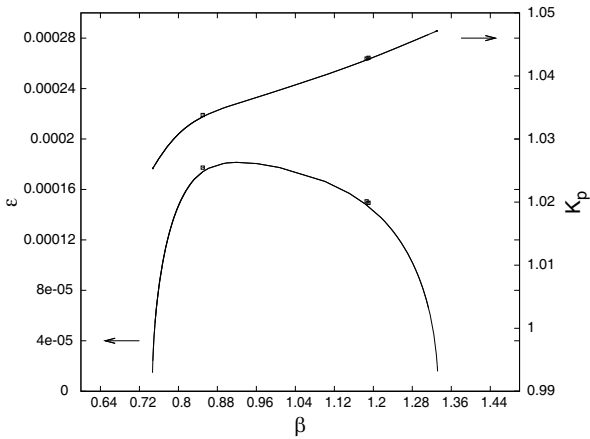


Fig. 16. Envelope of the spanwise wave number β for $Re = 291$ and $\alpha = 0.20$ for truncation $(5, 80, 5)$. The lowest value of β is 0.747 . The lower curve shows ϵ as a function of β , the values of K_p are given by the upper curve. A truncation of $(7, 100, 7)$ is used to confirm the solution curve (squares). The solutions at $\beta = 0.751, 0.850, 0.961, 1.100, 1.252$ and 1.321 are chosen for searching for the length of the streamwise domain L_x^* used in [25], *i.e.* the equivalent α . These values of β will later be used for locating optimal values of α for rendering it possible to lower the Reynolds number as much as possible, cf. fig. 19.

not close to the one used in [25] of 0.365 . Choosing six values of $\beta = 0.751, 0.850, 0.961, 1.100, 1.252$ and 1.321 we investigate the possibility of bringing the streamwise wave number α to the target values used in Biau [25] (*i.e.* $\alpha = 0.122$ and 0.209). At this Re the range in α is narrow over the whole range of β 's and therefore the lower target value of $\alpha = 0.122$ is not reachable, the lowest turned out to be 0.191 , while it is possible to bring α to the larger target value of 0.209 . To see whether or not these two values of α (and the solution at $\alpha = 0.20$) render the flow close to that of Biau in terms of the $\max[u_{rms}]$ we keep the Re fixed to 291 and α fixed to $0.191, 0.20$ and 0.209 , and map out the solutions in β . Looking back to fig. 15 one finds the $\max[u_{rms}]$ of the whole envelope in β for the three values of α . It is clear that the TWS of the preset symmetry do not make it to the target value or the maximum $u_{rms} = 0.12$ of [25], and do not survive down to the same spanwise wave number used by Biau ($= 0.365$). The TWS nearest to the target value of $\max[u_{rms}]$ is situated at 0.07 for $(\alpha, \beta) = (0.200, 1.332)$ whose 4-vortex velocity is rather featureless and do not match well that by Biau. The resulting velocity fields averaged over x for the same α and $\beta = 0.75$ and 0.93 (close to the lower limit in β , see fig. 16) are shown in fig. 17 and show a more characteristic velocity field with low- and high-speed streaks composed of 8 and 4 vortices respectively. Even though the two selected TWS are both of low amplitudes and do not match well the root-mean-square velocities of the chaotic dynamics on the separatrix, nor the shape factor of the periodic orbit, the spatial distribution of the TWS in terms of the streaky flow has some resemblance to the chaotic state shown in fig. 6 of Biau. Table 4 shows a comparison between the TWS of the present study and the edge states of [25] at $Re = 291$.

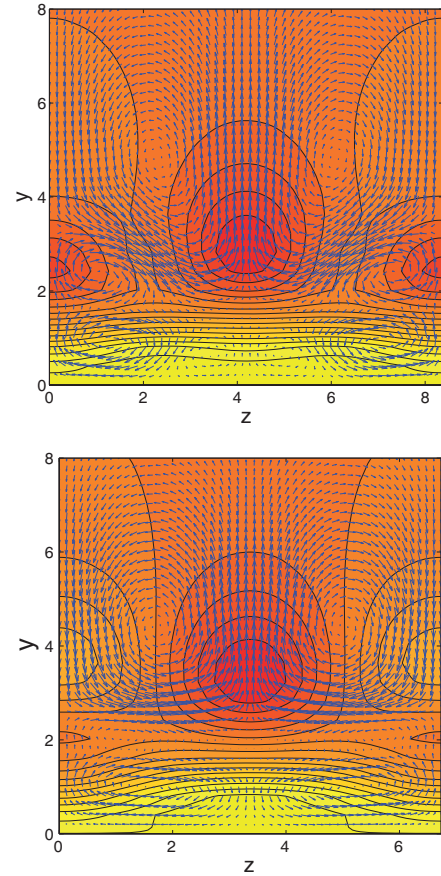


Fig. 17. Two velocity fields of the perturbation at $Re = 291$ and $\alpha = 0.20$. Top: the 8-vortex flow at $\beta = 0.75$ with an amplitude of the flow averaged over x equal to $|\bar{u}^x| = 0.037$ and the cross-flow $|\bar{v}^x| = 3.13 \cdot 10^{-4}$. For this flow we have the shape factor $H = 2.578$ and the mean spanwise spacing between the streaks $z^+ = 83$. Bottom: increasing only slightly the β to 0.93 the flow changes to a 4-vortex flow with a shape factor of 2.577 , $z^+ = 67$ and mean flow amplitudes equal to $|\bar{u}^x| = 0.054$ and $|\bar{v}^x| = 9.80 \cdot 10^{-4}$. Both flow states are of low amplitude and do not reach that of [25] in terms of the maximum of the root-mean-square velocities of the rather chaotic dynamics on the separatrix ($\max[u_{rms}] = 0.12$) or the span of shape factor $2.26 \leq H(t) \leq 2.49$ of the periodic orbit. Dark/red patches correspond to negative flow and the bright ones to positive flow away from the laminar flow.

Table 4. Properties of a selection of travelling wave solutions (top 3 rows) shown in fig. 15 compared to the edge state solution of [25] (row 4 and 5) at $Re = 291$. The 4th row corresponds to the seemingly chaotic flow, where the span of H is read off from fig. 4 of [25] and the 5th row is the periodic orbit. The wave speed c of the TWS is, from the first to the third row: $0.428, 0.442$ and 0.442 .

α	β	u_{rms}	K_p	z^+	ϵ	H
0.191	0.823	0.055	1.027	76	$8.8 \cdot 10^{-6}$	2.58
0.200	1.332	0.070	1.047	47	$1.6 \cdot 10^{-5}$	2.56
0.209	1.249	0.065	1.042	50	$2.6 \cdot 10^{-5}$	2.57
0.122	0.365	0.120	N/A	N/A	N/A	2.12-2.46
0.209	0.365	N/A	N/A	N/A	N/A	2.26-2.49

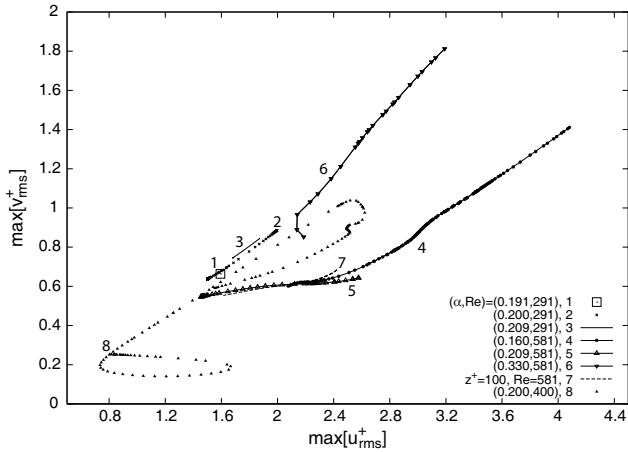


Fig. 18. Turbulence intensities represented by the root-mean-square velocity fluctuations $\max[u_{\text{rms}}^+]$ and $\max[v_{\text{rms}}^+]$ normalised by the friction velocity \hat{u}_τ according to eq. (18). The figure shows the same envelope of the spanwise wave number β at $Re = 400$ and $\alpha = 0.20$ shown in fig. 9 and for the envelope in β of the solutions of various α 's at $Re = 291$ and 581 shown in fig. 15. The legends give the value of the Re and the α . The square symbol \square represents several solutions of a very short envelope.

In laboratory experiments turbulence statistics or intensities are often measured in terms of the maximum of the root-mean-square velocities normalised by the friction velocity \hat{u}_τ , see eq. (18). We here use the $\max[u_{\text{rms}}^+]$ and $\max[v_{\text{rms}}^+]$ to represent the nonlinear TWS, each flow state is a point in fig. 18 for the Reynolds numbers considered so far, *i.e.* $Re = 291, 400$ and 581 . The figure shows statistics of the solutions for which convergence could be confirmed with a higher truncation, and also, having $K_p \leq 1.30$. The maximum of the root-mean-square velocities of the TWS presented here is situated more or less in the same region as that of the simulation of turbulence of [85], having $(\max[u_{\text{rms}}^+], \max[v_{\text{rms}}^+]) \approx (2.6, 1.1)$, and the compilation of several works in [86] showing root-mean-square velocities of equilibrium states and periodic orbits of various flow configurations. The present TWS, of the imposed symmetry and for the given values of α , are mildly streak-dominated (*i.e.* $\max[u_{\text{rms}}^+] > \max[v_{\text{rms}}^+]$) and never reach as high $\max[u_{\text{rms}}^+]$ as the particularly strongly streak-dominated twofold rotationally symmetric travelling waves of pipe flow [43, 51, 87] at $(\max[u_{\text{rms}}^+], \max[v_{\text{rms}}^+]) \approx (7, 0.9)$.

Search for the minimum Reynolds number

To find the global minimum point in Re of the travelling waves the search starts from the already known solution at $Re = 291$. In this way we get an indication of where the Blasius flow is a global attractor and from where it starts to cohabit the phase space with the travelling wave solutions. We use again as starting points the same six values of β extracted from the solution curve shown in fig. 16 and map out the solutions in α to find the point that yields the

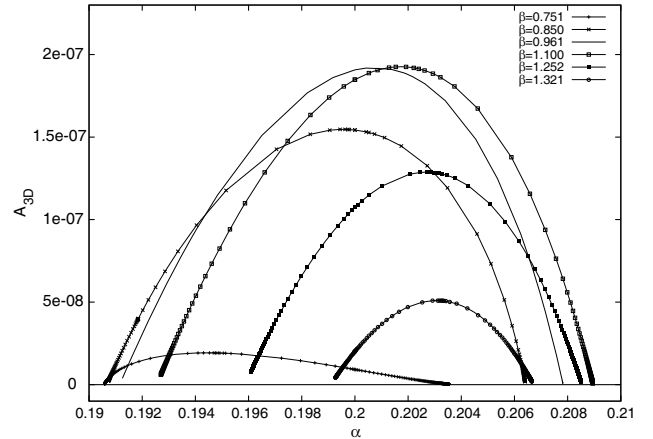


Fig. 19. Envelope in α for $Re = 291$ and $\beta = 0.751, 0.850, 0.961, 1.100, 1.252$ and 1.321 . The points corresponding to $\max[A_{3D}]$ of each curve are used as starting points for finding which combination of α and β minimises the Reynolds number.

largest value of the A_{3D} , see eq. (15) and fig. 19. Having found the maximum point in A_{3D} of each curve we choose those combinations of α and β to continue in Re with the aim to reach the lowest possible value. In this manner we find that the $\min[Re] = 288.1$ for $(\alpha, \beta) = (0.200, 0.961)$, where the solution is still three-dimensional, cf. fig. 20. A small difference in Re of approximately 0.20 is seen for the solutions of the other combinations of α and β at slightly larger Re , hence indicating that $Re = 288.1$ is a good estimate of the minimum Reynolds number. Based on the displacement thickness this translates to $Re_* = 495.8$ and $(\alpha_*, \beta_*) = (0.344, 1.654)$. Whether other forcings would bring the Re to an even lower value remains to be established. In other flow configurations, such as the circular pipe flow, turbulence is maintained at around $Re = 2000$ whereas the lower limit known so far of the travelling wave solutions extend to more than half of that at $Re = 773$, computed by [55]. In a similar fashion and knowing that the lower limit of sustained turbulence for the Blasius boundary layer flow is around $Re = 232$ (or $Re_* = 400$) according to [25] and [31] it is possible that the given $\min[Re] = 288.1$ may not necessarily be the absolute minimum. For the solution at the Reynolds number defined as $\min[Re]$ we have $\epsilon = 5.22 \cdot 10^{-6}$ giving an amplitude of the mean flow of the perturbation averaged over x of $|\bar{u}^x| = 0.037$ and $|\bar{v}^x| = 2.66 \cdot 10^{-5}$, while the amplitude measure of the wavy part is $A_{3D} = 2.84 \cdot 10^{-5}$. At this point the solution is still three-dimensional but close to the laminar flow with the shape factor H equal to 2.574 and the correction coefficient $K_p = 1.031$. Starting from this solution the flow bifurcates supercritically towards larger Re . Figure 21 shows the 4-vortex velocity field averaged over x representing the flow at $Re = \min[Re]$. Since the flow is still three-dimensional at this subcritical Re one might wonder how it relates to the laminar Blasius flow. This leads one to think of a possible connection to optimal perturbations. Since these states are initial optimal states at $t = 0$, computed to produce maximum energy growth at a predetermined time T , it is speculated that they evolve

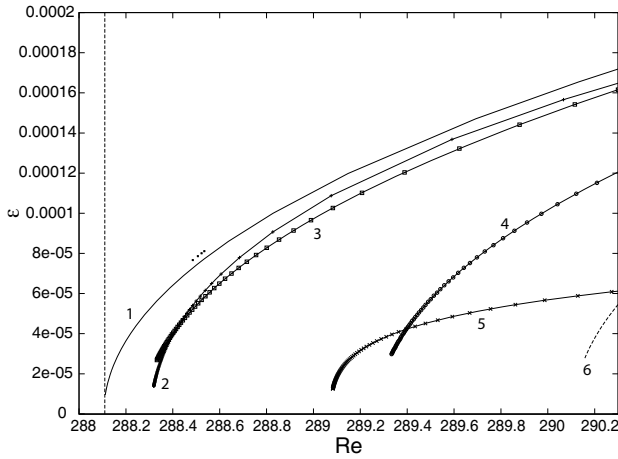


Fig. 20. Search of the $\min[Re]$ by considering various fixed combinations of α and β , using a truncation of $(NX, NY, NZ) = (5, 80, 5)$. The numbered curves 1-6 correspond to the following combinations of α and β : 1 (0.2004, 0.9613), 2 (0.1994, 0.8500), 3 (0.2015, 1.1006), 4 (0.2026, 1.2515), 5 (0.1945, 0.7505) and 6 (0.2031, 1.3210). For $\alpha = 0.2004$ and $\beta = 0.9613$ the curve can be brought down to $Re = 288.1$ as shown, which is the minimum value found. For this combination of α and β and beyond a certain point the Re hardly changes, after more than 200 solutions from this point onwards the continuation is terminated since Re changes only on its third digit. In this way we finally arrive at the point we define as the minimum point in Re , or $\min[Re] = 288.1$. The solution curve 1 is confirmed at a few Re using a higher truncation of $(7, 100, 7)$ represented by the black dots.

in time towards the attracting TWS possibly embedded in the edge of chaos. Looking at the known linear optimal perturbations of [36] at $Re_* = 610$, a flow characterized by a counter rotating 2-vortex state in the cross-sectional plane is found, having a certain dependency on the streamwise direction x . This has some similarity to the present x -dependent TWS also represented by a 2-vortex flow and likewise situated within a periodic box at the same Reynolds number. However, the linear optimal state is localised in z which the TWS is not. Looking at the known nonlinear optimal perturbations of [88] the match is quite poor with the optimal solution again being local in z . The edge state solution in the similar study of the asymptotic suction boundary layer by [60] suggests of a travelling wave like behaviour. The flow studied therein corresponds to $Re_* = 400$ (based on the displacement thickness) which shows an edge state periodic in time, and the velocity field averaged over the streamwise distance has some resemblance to the TWS shown in fig. 21. However, their edge state solution has a shift-and-reflect symmetry while our TWS obeys a reflect symmetry along $z = 0$. To summarise the discussion of the flow at the lowest Reynolds number, table 5 presents some information of this particular solution showing, in particular, that the amplitude of the streamwise root-mean-square velocity is less than 6% of the free-stream velocity.

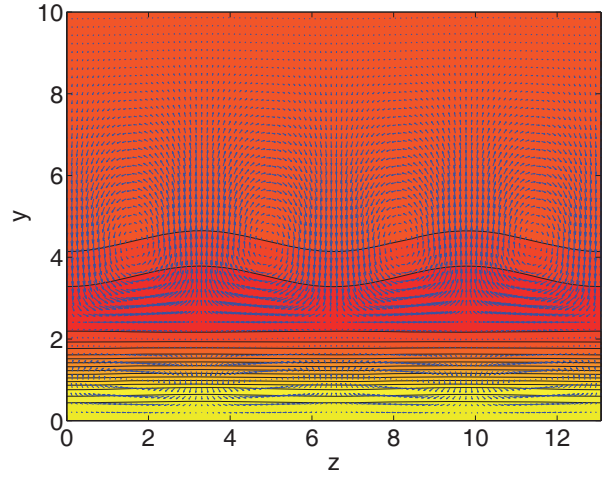


Fig. 21. The velocity field averaged over x at the lowest $Re = 288.1$ at $(\alpha, \beta) = (0.200, 0.961)$. The velocity field corresponds to two periods in z and has some resemblance to the time-periodic edge state solution of [60] for the asymptotic suction boundary layer.

Table 5. Properties of the travelling wave solution at $Re = 288.1$, $(\alpha, \beta) = (0.200, 0.961)$ for a truncation of $(NX, NY, NZ) = (5, 80, 5)$. The values of the root-mean-square velocities refer to their maximum.

z^+	u_{rms}	v_{rms}	u_{rms}^+	v_{rms}^+	c
65	$5.71 \cdot 10^{-2}$	$2.47 \cdot 10^{-2}$	1.657	0.716	0.434

4 Floquet analysis of the ECS

To get insight into the relevance of the ECS found here their linear stability is studied using Floquet theory, which is a useful tool for classifying and computing various types of instabilities. The information sought for is merely to extract from the stability analysis whether or not the ECS are unstable. Below we present the general secondary perturbation \mathbf{u}' superimposed on the nonlinear (X, y, z) -dependent base flow \mathbf{u}_{ECS} consisting of the Blasius flow ($K_p f'(\eta)$) plus the ECS (see eq. (23)). We consider the flow in a moving frame of reference where the ECS is steady. According to [89] the linear perturbation imposed on the nonlinear base flow has the following general expression:

$$\mathbf{u}'(\mathbf{x}, t) = e^{-I\vartheta t} \sum_{m=-NX_2}^{NX_2} \sum_{n=-NZ_2}^{NZ_2} \tilde{\mathbf{u}}^{(mn)}(y) \times e^{I(n\beta+\xi)z} e^{I(m\alpha+\zeta)X}, \quad (28)$$

where $\mathbf{x} = (X, y, z)$ and $\tilde{\mathbf{u}}^{(mn)}(y)$ is represented by NY_2 Chebyshev polynomials. We are interested in the temporal growth of \mathbf{u}' , hence we set both ξ and ζ real while ϑ is complex in general. The ECS is unstable for $\vartheta_i > 0$. Since turbulent flow have shown to correspond to $z^+ = 100$ [76] we perform a linear stability analysis of the previously mentioned solutions at $(\alpha, \beta, Re) = (0.16, 0.733, 400)$ and

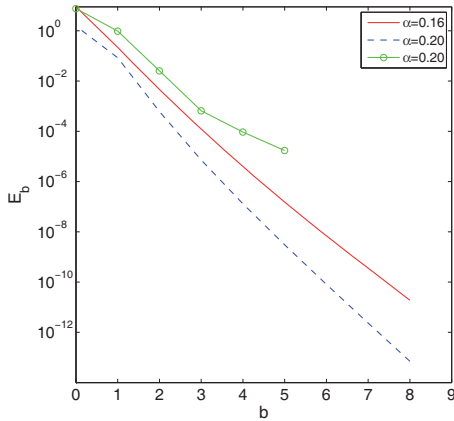


Fig. 22. The energy content E'_b as a function of the Fourier modes $b = 0, 1, 2, \dots, NX$ with $(\alpha, \beta, Re) = (0.16, 0.733, 400)$ for the solid line; $(0.20, 0.728, 400)$ dashed line and $(0.200, 0.961, 288)$ circles. The dominant mode is the x -independent component, *i.e.* the Fourier mode $b = 0$.

$(0.20, 0.728, 400)$ having that particular value of z^+ , plus the solution at $\min[Re] = 288$ having $\alpha = 0.200$ and $\beta = 0.961$. Those solutions have fairly low values of α , *i.e.* a slow development in x , they are situated on the lower branch in the wave amplitude $A_{3D}(\beta)$ system (*i.e.* the amplitude measure of the wavy X -dependent part of the perturbation) shown in *e.g.* fig. 9. In this stability analysis we use as a base flow the Blasius flow plus the mean ECS integrated over X . This is justified in fig. 22 showing a comparison of the energy content E'_b of each Fourier mode b of the ECS. The ratio of the energy between the mean flow integrated over X (*i.e.* the $b = 0$ component) and the wavy part (*i.e.* the sum of the energy contribution E'_b from each Fourier component $b = 1, 2, \dots, NX$) is approximately 40 for the $\alpha = 0.16$ -solution, 20 for the solution at $\alpha = 0.20$ and 10 for the solution at $Re = 288$. This implies that the majority of the energy is contained in the x -independent part (*i.e.* the Fourier mode $b = 0$). Having this in mind we perform a linear stability analysis of the (y, z) -dependent flow or the Blasius flow plus the X -independent part of the ECS, thus also simplifying the numerical representation of \mathbf{u}' keeping $NX_2 = 1$ and $\zeta = 0$. Parameters with subscripts 2 refer to the secondary perturbation in order to distinguish them from those of the ECS. The range studied in the streamwise wave number α_2 is 0.12, 0.20 and 1, with β kept invariant with $\xi = 0$ (*i.e.* we do not look for detuned solutions). The two base flows having $z^+ = 100$ are found to be weakly unstable for $\alpha_2 = 0.20$, with only one unstable direction, which goes along with the stability characteristic of computed TWS in other flow configurations. The solution at $Re = 288$ is found to be stable for all perturbations considered. Tables 6 and 7 present the eigenvalues ϑ of the two unstable base flow solutions, starting with the largest growth rate ϑ_i and then in descending order. The rather simple globally periodic TWS can serve as a platform from where more complex flows (such as periodic orbits) can take off. Unstable periodic orbits are be-

Table 6. Linear secondary stability results of the ECS with $(\alpha, \beta, Re) = (0.16, 0.733, 400)$ for $\xi = 0$ and $\zeta = 0$. Two truncations are used to confirm convergence; the eigenvalues below correspond to the highest resolution $(NX_2, NY_2, NZ_2) = (1, 100, 6)$. For $\alpha_2 = 0.20$ there is a weakly unstable mode with positive growth rate $\vartheta_i = 0.00076$.

α_2	ϑ
0.20	$0.07573 + 0.00076i$
	$0.08486 - 0.01757i$
	$0.12089 - 0.01941i$

Table 7. Linear secondary stability results of the ECS with $(\alpha, \beta, Re) = (0.20, 0.728, 400)$ for $\xi = 0$ and $\zeta = 0$. Two truncations are used to confirm convergence; the eigenvalues below correspond to the highest resolution $(NX_2, NY_2, NZ_2) = (1, 120, 8)$. For $\alpha_2 = 0.20$ there is a weakly unstable mode with positive growth rate $\vartheta_i = 0.00082$.

α_2	ϑ
0.20	$0.07673 + 0.00082i$
	$0.08466 - 0.02004i$
	$0.04664 - 0.02481i$

lieved to be the skeleton of chaotic dynamics according to the periodic orbit theory [72, 90]. The application of cycle expansions on various low-dimensional chaotic dynamical systems has been tested in the past by *e.g.* [91] and recently on two-dimensional turbulence by [59], where exact recurrent flows were extracted from numerical simulations and then used as building blocks to successfully reproduce turbulence statistics.

5 Conclusions

Applying the parallel flow assumption of the laminar Blasius flow, nonlinear exact coherent structures of a preset symmetry, $(u, v, w, p) = (u, v, -w, p)$ as $z \rightarrow -z$, are discovered and mapped out in the streamwise and the spanwise wave number space for a few values of the Reynolds number. One value of Re is set close to the critical value for linear instability of Tollmien-Schlichting waves in order to look into the presence of alternative solutions in phase space, and two different Reynolds numbers are chosen to look into the relevance of nonlinear travelling waves to the edge state computed by Biau [25]. There are other solutions to search for, such as those corresponding to the shift-and-reflect symmetry, $(u, v, w, p) = (u, v, -w, p)$ as $x \rightarrow x + \pi/\alpha$ and $z \rightarrow -z$, used several times in other canonical flows. This is left out for future studies. In this study we have determined a new limit in phase space where nonlinear travelling wave solutions, consisting of 4-vortices, set in at $Re = 288$ or $Re_* = 496$ (based on the displacement thickness) having an streamwise root-mean-square velocity of up to 6% of the free-stream velocity. To put this solution in comparison to other already known limits we have the threshold for monotonic

decay at $Re_* = 17$, the lower limit of sustained turbulence at $Re_* = 400$ and the critical Reynolds number for growth of linear Tollmien-Schlichting waves at $Re_* = 520$. At the computed subcritical minimum point the three-dimensional exact coherent structures identified bifurcate supercritically. Some of the selected states presented herein possess the same spanwise spacing as experimental turbulence and are found to be unstable to small amplitude perturbations through a Floquet analysis. Computing the shape factor H it is realised that the solutions are not turbulent but are close to the laminar state. Their values of H match better the time-periodic edge state structures computed in the transitional study of Biau [25]. Fixing the mean streamwise spacing z^+ to 100 and the Reynolds number to the same value as Biau it is found that the solutions compare well in the streamwise wave length but poorly in the spanwise direction, giving $H = 2.57$ for the travelling wave presented here. Removing the restriction of $z^+ = 100$ the TWS compare better, in terms of turbulent statistics, to Biau and also to TWS computed for other flow configurations. The instability of the exact coherent structures reported herein makes them interesting from a dynamical system point of view where transition to turbulence can be interpreted as a walk in phase space among unstable solutions. Whether or not the discovered solutions are of importance should be tested through numerical simulations and laboratory experiments. The numerical work could consist in using the ECS and its unstable manifold as an initial condition and then march the Navier-Stokes equations forward in time to examine the flow trajectory. Another reason for testing the solutions using a time-stepper would be for verifying the parallel flow assumption used here and the use of the correction coefficient K_p for ensuring the correct asymptotic behaviour of the solutions in the wall-normal direction. Attaining a better knowledge of the ECS and its unstable directions and their role in phase space, *i.e.* the possible connections with the laminar or the turbulent state, might lead to ideas on how to relaminarise the flow by forcing a trajectory onto the laminar unstable manifold of the ECS. Since the present study is the very first step in the study of the transition to turbulence in the Blasius boundary layer, further numerical work needs to be carried out. The next step would be to increase the family of nonlinear solutions of the Navier-Stokes equations. The travelling waves are interesting and offer glimpses of states visited by chaotic flows [52, 57]; however, one does not see the bursting phenomenon (*i.e.* strong erratic ejections of low-speed fluid from the region next to the plate) by solely looking at the TWS. To do this one needs to search for generic periodic orbits.

The financial support of a European Re-integration Grant (ERG) No. 268265 is gratefully acknowledged. The authors wish to thank Prof. John Burkhardt, Dr. Damien Biau and Dr. Stefania Cherubini for interactions and advice. The careful and very insightful comments by both anonymous referees are greatly appreciated.

References

1. O. Reynolds, Philos. Trans. **174**, 935 (1883).
2. H.J. Poincaré, Acta Math. **13**, 1 (1890).
3. L.D. Landau, C. R. Dokl. Acad. Sci. USSR **44**, 311 (1944).
4. E. Hopf, Commun. Pure Appl. Math. **1**, 303 (1948).
5. D. Ruelle, F. Takens, Commun. Math. Phys. **20**, 167 (1971).
6. S. Newhouse, D. Ruelle, F. Takens, Commun. Math. Phys. **64**, 35 (1978).
7. E. Ott, in *Chaos in Dynamical Systems* (Cambridge University Press, 1993).
8. J.P. Gollub, H.L. Swinney, Phys. Rev. Lett. **35**, 927 (1975).
9. E.N. Lorenz, J. Atmos. Sci. **20**, 130 (1963).
10. S.H. Strogatz, in *Nonlinear Dynamics and Chaos: With Applications to Physics, Biology, Chemistry, and Engineering (Studies in Nonlinearity)* (Westview Press, 2001).
11. Y. Pomeau, P. Manneville, Commun. Math. Phys. **74**, 189 (1980).
12. P.G. Drazin, W.H. Reid, in *Hydrodynamic Stability* (Cambridge University Press, 1981).
13. A. Meseguer, L.N. Trefethen, J. Comput. Phys. **186**, 178 (2003).
14. A.G. Darbyshire, T. Mullin, J. Fluid Mech. **289**, 83 (1995).
15. B. Hof, A. Juel, T. Mullin, Phys. Rev. Lett. **91**, 244502 (2003).
16. T. Mullin, J. Peixinho, in *Proceedings of the Sixth IUTAM Symposium on Laminar-Turbulent Transition* (Springer, Dordrecht, 2006) pp. 45–55.
17. J. Peixinho, T. Mullin, J. Fluid Mech. **582**, 169 (2007).
18. J. Peixinho, T. Mullin, Phys. Rev. Lett. **96**, 094501 (2006).
19. A.P. Willis, R.R. Kerswell, Phys. Rev. Lett. **98**, 014501 (2007).
20. K. Avila, D. Moxey, A. de Lozar, M. Avila, D. Barkley, B. Hof, Science **333**, 192 (2011).
21. S. Toh, T. Itano, J. Fluid Mech. **481**, 67 (2003).
22. T.M. Schneider, B. Eckhardt, J.A. Yorke, Phys. Rev. Lett. **99**, 034502 (2007).
23. T.M. Schneider, J.F. Gibson, M. Lagha, F. De Lillo, B. Eckhardt, Phys. Rev. E **78**, 037301 (2008).
24. Y. Duguet, A.P. Willis, R.R. Kerswell, J. Fluid Mech. **613**, 255 (2008).
25. D. Biau, Phys. Fluids **24**, 034107 (2012).
26. S. Cherubini, P. De Palma, J.C. Robinet, A. Bottaro, Phys. Fluids **23**, 051705 (2011).
27. Y. Duguet, P. Schlatter, D.S. Henningson, B. Eckhardt, Phys. Rev. Lett. **108**, 044501 (2012).
28. P.J. Schmid, D.S. Henningson, in *Stability and Transition in Shear Flows* (Springer, 2001).
29. H. Fasel, U. Konzelmann, J. Fluid Mech. **221**, 311 (1990).
30. G.B. Klingmann, A.V. Boiko, K.J.A. Westin, V.V. Kozlov, P.H. Alfredsson, Eur. J. Mech. B/Fluids **12**, 493 (1993).
31. P.R. Spalart, J. Fluid Mech. **187**, 61 (1988).
32. P. Andersson, Martin Berggren, D.S. Henningson, Phys. Fluids **11**, 134 (1999).
33. K.M. Butler, B.F. Farrell, Phys. Fluids A **4**, 1637 (1992).
34. S. Zuccher, A. Bottaro, P. Luchini, Eur. J. Mech. B/Fluids **25**, 1 (2006).
35. S. Cherubini, P. De Palma, J.-Ch. Robinet, A. Bottaro, Phys. Rev. E **82**, 066302 (2010).
36. S. Cherubini, J.-Ch. Robinet, A. Bottaro, P. De Palma, J. Fluid Mech. **656**, 231 (2010).

37. D. Biau, H. Soueid, A. Bottaro, J. Fluid Mech. **596**, 133 (2008).
38. S.J. Kline, W.C. Reynolds, F.A. Schraub, P.W. Runstadler, J. Fluid Mech. **30**, 741 (1967).
39. F. Waleffe, Phys. Fluids **9**, 883 (1997).
40. F. Waleffe, J. Fluid Mech. **435**, 93 (2001).
41. F. Waleffe, Phys. Fluids **15**, 1517 (2003).
42. H. Faisst, B. Eckhardt, Phys. Rev. Lett. **91**, 224502 (2003).
43. H. Wedin, R.R. Kerswell, J. Fluid Mech. **508**, 333 (2004).
44. C.C.T. Pringle, Y. Duguet, R.R. Kerswell, Philos. Trans. R. Soc. A **367**, 457 (2009).
45. H. Wedin, A. Bottaro, M. Nagata, *Advances in Turbulence XII, in Proceedings of the 12th EUROMECH European Turbulence Conference*, edited by B. Eckhardt (Philipps-Universität Marburg, Marburg, Germany, 2009) pp. 141–144.
46. H. Wedin, A. Bottaro, M. Nagata, Phys. Rev. E **79**, 065305 (2009).
47. M. Uhlmann, G. Kawahara, A. Pinelli, Phys. Fluids **22**, 084102 (2010).
48. T. Itano, S.C. Generalis, Phys. Rev. Lett. **102**, 114501 (2009).
49. M. Nagata, J. Fluid Mech. **217**, 519 (1990).
50. S. Okino, M. Nagata, H. Wedin, A. Bottaro, J. Fluid Mech. **657**, 413 (2010).
51. R.R. Kerswell, O.R. Tutty, J. Fluid Mech. **584**, 69 (2007).
52. B. Hof, C.W.H. Doorne, J. Westerweel, F.T.M. Nieuwstadt, H. Faisst, B. Eckhardt, H. Wedin, R.R. Kerswell, F. Waleffe, Science **305**, 1594 (2004).
53. B. Hof, C.W.H. van Doorne, J. Westerweel, F.T.M. Nieuwstadt, Phys. Rev. Lett. **95**, 214502 (2005).
54. A.P. Willis, R.R. Kerswell, Phys. Rev. Lett. **100**, 124501 (2008).
55. C.C.T. Pringle, R.R. Kerswell, Phys. Rev. Lett. **99**, 074502 (2007).
56. J. Wang, J. Gibson, F. Waleffe, Phys. Rev. Lett. **98**, 204501 (2007).
57. A. de Lozar, F. Mellibovsky, M. Avila, B. Hof, Phys. Rev. Lett. **108**, 214502 (2012).
58. G. Kawahara, S. Kida, J. Fluid Mech. **449**, 291 (2001).
59. G.J. Chandler, R.R. Kerswell, J. Fluid Mech. **722**, 554 (2013).
60. T. Kreilos, G. Veble, T.M. Schneider, B. Eckhardt, J. Fluid Mech. **726**, 100 (2013).
61. T. Khapko, T. Kreilos, P. Schlatter, Y. Duguet, B. Eckhardt, D.S. Henningson, J. Fluid Mech. **717**, R6 (2013).
62. J.M. Hamilton, J. Kim, F. Waleffe, J. Fluid Mech. **287**, 317 (1995).
63. F. Waleffe, Stud. Appl. Math. **95**, 319 (1995).
64. T.M. Schneider, J.F. Gibson, J. Burke, Phys. Rev. Lett. **104**, 104501 (2010).
65. M. Avila, F. Mellibovsky, N. Roland, B. Hof, Phys. Rev. Lett. **110**, 224502 (2013).
66. J.M. Rotenberry, Phys. Fluids A **5**, 1840 (1993).
67. F.A. Milinazzo, P.G. Saffman, J. Fluid Mech. **160**, 281 (1985).
68. W. Koch, J. Fluid Mech. **243**, 319 (1992).
69. U. Ehrenstein, M. Rossi, Phys. Fluids **8**, 1036 (1996).
70. U. Ehrenstein, W. Koch, Phys. Fluids **7**, 1282 (1995).
71. W. Koch, F.P. Bertolotti, A. Stolte, S. Hein, J. Fluid Mech. **406**, 131 (2000).
72. P. Cvitanović, J. Fluid Mech. **726**, 1 (2013).
73. M. Matsubara, P.H. Alfredsson, J. Fluid Mech. **430**, 149 (2001).
74. B.R. Munson, D.F. Young, T.H. Okiishi, W.W. Huebsch, in *Fundamentals of Fluid Mechanics*, 6th edition (Wiley, 2010).
75. C. Canuto, M.Y. Hussaini, A. Quarteroni, T.A. Zang, in *Spectral Methods in Fluid Dynamics* (Springer-Verlag, 1988).
76. S.K. Robinson, Annu. Rev. Fluid Mech. **23**, 601 (1991).
77. C.R. Smith, S.P. Metzler, J. Fluid Mech. **129**, 27 (1983).
78. H. Wedin, D. Biau, A. Bottaro, M. Nagata, Phys. Fluids **20**, 094105 (2008).
79. W.C. Rheinboldt, J.V. Burkardt, ACM Trans. Math. Software **9**, 236 (1983).
80. W.C. Rheinboldt, J.V. Burkardt, ACM Trans. Math. Software **9**, 215 (1983).
81. U. Ehrenstein, W. Koch, J. Fluid Mech. **228**, 111 (1991).
82. W. Koch, *Nonlinear Instability of Nonparallel Flows*, edited by S.P. Lin, W.R.C. Phillips, D.T. Valentine (Springer-Verlag, Berlin, 1994) pp. 117–126.
83. D. Biau, A. Bottaro, Philos. Trans. R. Soc. A **367**, 529 (2009).
84. S. Okino, M. Nagata, J. Fluid Mech. **693**, 57 (2012).
85. J. Kim, P. Moin, R. Moser, J. Fluid Mech. **177**, 133 (1987).
86. G. Kawahara, M. Uhlmann, L. van Veen, Annu. Rev. Fluid Mech. **44**, 203 (2012).
87. R.R. Kerswell, Nonlinearity **18**, R17 (2005).
88. S. Cherubini, P. De Palma, J.C. Robinet, A. Bottaro, J. Fluid Mech. **689**, 221 (2011).
89. T. Herbert, Annu. Rev. Fluid Mech. **20**, 487 (1988).
90. P. Cvitanović, R. Artuso, R. Mainieri, G. Tanner, G. Vattay, in *ChaosBook.org* (Niels Bohr Institute, 2013).
91. R. Artuso, E. Aurell, P. Cvitanović, Nonlinearity **3**, 361 (1990).